

# Radio emission from a pulsar's magnetic pole revealed by general relativity

Gregory Desvignes,<sup>1,2\*</sup> Michael Kramer,<sup>1,3</sup> Kejia Lee,<sup>4</sup> Joeri van Leeuwen,<sup>5,6</sup>  
Ingrid Stairs,<sup>7</sup> Axel Jessner,<sup>1</sup> Ismaël Cognard,<sup>8,9</sup> Laura Kasian,<sup>7</sup>  
Andrew Lyne,<sup>3</sup> Ben W. Stappers<sup>3</sup>

<sup>1</sup>Max-Planck-Institut für Radioastronomie, Auf dem Hügel, 69 D-53121 Bonn, Germany

<sup>2</sup>Laboratoire d'Études Spatiales et d'Instrumentation en Astrophysique, Observatoire de Paris,  
Université Paris-Sciences-et-Lettres, Centre National de la Recherche Scientifique, Sorbonne Université,  
Université de Paris, 5 place Jules Janssen, 92195 Meudon, France

<sup>3</sup>Jodrell Bank Centre for Astrophysics, School of Physics and Astronomy,  
The University of Manchester, Manchester M13 9PL, UK

<sup>4</sup>Kavli institute for astronomy and astrophysics, Peking University,  
Beijing 100871, People's Republic of China

<sup>5</sup>ASTRON, The Netherlands Institute for Radio Astronomy,  
Postbus 2, 7990 AA Dwingeloo, The Netherlands

<sup>6</sup>Astronomical Institute Anton Pannekoek, University of Amsterdam,  
Science Park 904, 1098 XH Amsterdam, The Netherlands

<sup>7</sup>Department of Physics and Astronomy, University of British Columbia,  
Vancouver, BC V6T 1Z1, Canada

<sup>8</sup>Laboratoire de Physique et Chimie de l'Environnement et de l'Espace,  
Centre National de la Recherche Scientifique-Université d'Orléans, F-45071 Orléans, France

<sup>9</sup>Station de radioastronomie de Nançay, Observatoire de Paris,  
Centre National de la Recherche Scientifique,  
Institut national des sciences de l'Univers, F-18330 Nançay, France

\*To whom correspondence should be addressed; E-mail: gdesvignes@mpifr-bonn.mpg.de.

**Binary pulsars are affected by general relativity (GR), causing the spin axes**

**of each pulsar to precess. We present polarimetric radio observations of PSR J1906+0746 that demonstrate the validity of the geometrical model of pulsar polarisation. We reconstruct the (sky-projected) polarisation emission map over the pulsar’s magnetic pole and predict the disappearance of the detectable emission by 2028. Two additional tests of GR are performed in this system, including the spin-precession for strongly self-gravitating bodies. We constrain the relativistic treatment of the pulsar polarisation model and measure the pulsar beaming fraction, with implications for the population of neutron stars and the expected rate of neutron star mergers.**

Pulsars are fast-spinning neutron stars of mass  $\sim 1.2 - 2.2$  solar masses ( $M_{\odot}$ ) with strong magnetic fields that emit a beam of radio waves along their magnetic axes above each of their opposite magnetic poles. Einstein’s theory of general relativity (GR) predicts that space-time is curved by massive bodies. Predicted effects of this include relativistic spin-precession in binary pulsars (*1*). This precession arises from any misalignment, by an angle  $\delta$ , of the spin vector of each pulsar with respect to the total angular momentum vector of the binary, most likely caused by an asymmetric supernova explosion imparting a kick onto (one of) the neutron star(s) (*2, 3*). This precession causes the viewing geometry to vary, which can be tested observationally.

As a pulsar rotates, its radio beams sweep the sky. If one of the beams crosses our line of sight (LOS), its emission is perceived as being pulsed, that, when averaged over several hundreds of pulsar rotations, typically forms a stable pulse profile. Evidence for a variable pulse profile attributed to changes in the viewing geometry caused by spin-precession have been observed and modelled for the binary pulsar B1913+16 (*4, 5*). Polarisation information can provide an additional and independent tool to study relativistic spin-precession (*6, 7*). We expect that the position angle (PA) sweep of a pulsar’s linearly polarised emission due to geometrical effects can be described by the Rotating Vector Model (RVM) (*8*). This simple model, which

assumes a magnetic dipole centred on the pulsar, relates the PA to the projection of the magnetic field line direction as the pulsar beam rotates and crosses our LOS. The resulting gradient of the PA sweep as a function of the pulsar rotational phase (9) depends only on the magnetic inclination angle  $\alpha$  and the impact parameter  $\beta$  (i.e. the angle of closest approach between the observer direction and the magnetic axis). For LOSs crossing opposite sides of the same magnetic pole, the RVM predicts opposite slopes of the PA swing, which becomes steeper for smaller  $\beta$  (10). RVM has been extended to include rotational and relativistic effects between the pulsar and observer frame (11, 12), in principle allowing emission heights for the observed radio emission to be estimated. Although the RVM matches observations of young pulsars that present a smooth PA swing (13), deviations are also observed, so for large emission heights the pure dipole approximation may not be valid for a rotating plasma-loaded magnetosphere (14). Evidence for the central assumption of all these models, i.e. the geometrical meaning of the PA sweep, has so far been missing.

When PSR J1906+0746 (position  $19^{\text{h}}06^{\text{m}}48.86^{\text{s}} + 07^{\circ}46'25.9''$ , J2000 equinox), a young pulsar with spin period  $P_{\text{S}} \sim 144$  ms in a 4-hr orbit around an other neutron star, was discovered in 2004 (15), it showed two polarised emission components separated by nearly half a period (or  $\sim 180$  deg of pulse longitude). The “main pulse” (MP) and “interpulse” (IP) indicated a nearly orthogonal geometry where emission from both magnetic poles is visible from Earth. Comparison with archival data from the Parkes Multibeam Pulsar Survey (PMPS) (16) revealed that only the stronger MP had been visible in 1998 (15), suggesting effects of relativistic spin precession. Timing analysis of this pulsar (17) has measured three relativistic corrections to the orbit, the Post-Keplerian (PK) parameters. Two of the PK parameters, the periastron advance  $\dot{\omega}$  and the time dilation  $\gamma$ , allow us to determine a pulsar and companion mass of  $m_{\text{p}} = 1.29 \pm 0.01 M_{\odot}$  and  $m_{\text{c}} = 1.32 \pm 0.01 M_{\odot}$ , respectively, assuming GR is correct. The third PK parameter, the orbital decay due to gravitational wave emission  $\dot{P}_{\text{b}}$ , is consistent with these

measurements, providing a 5% test of GR (17). GR also provides an estimate of the orbital inclination angle  $i = 43.7 \pm 0.4^\circ$  or  $136.3 \pm 0.4^\circ$  (due to a  $180^\circ$  degeneracy) and the spin precession rate  $\Omega_p = 2.234 \pm 0.014^\circ \text{ yr}^{-1}$ . Independent measurements of these two terms are potentially observable in precessing systems, allowing these GR predicted values to be tested. Observations of the Double Pulsar (18) and PSR B1534+12 (7, 19) match the GR predictions of spin-precession with precisions of 13% and 20%, respectively.

We have monitored PSR J1906+0746 from 2012-18 with the 305-m William E. Gordon Arecibo radio telescope using the Puerto Rico Ultimate Pulsar Processing Instrument (PUPPI) tuned at a central frequency of 1.38 GHz. We supplement those observations with archival data from the Nançay and Arecibo telescopes recorded between 2005 and 2009 (17, 20). In total, our dataset comprises 47 epochs spanning from July 2005 to June 2018.

A previously observed trend of changing separation between MP and IP profiles with time (17), has continued. Our data shows that the slope of the PA under the MP gradually flattens with time, while the MP becomes simultaneously weaker and subsequently undetectable towards the end of 2016. This indicates that our LOS has moved out of the MP emission beam.

The progressive steepening of the PA curve under the IP eventually leads to a flip of the PA around May 2014 (although it appears flat due to the  $180^\circ$  ambiguity in the PA), followed by a flattening. This behaviour is in agreement with the RVM for a pole crossing our LOS. The observed change in the PA curve provides the evidence that the PA swing has a geometrical origin linked to the magnetic field.

The presence of MP and IP emission, covering a wide range of pulse longitudes, allows a precise determination of the viewing geometry as a function of time. We performed a simultaneous modelling of the polarimetric profiles using the RVM including the effects of relativistic spin-precession (21), hereafter referred to as the ‘precessional RVM’. A total of 53 parameters are included in this model (see Table S1); the main parameters are the angle between the ro-

tation axis and the magnetic axis of the MP,  $\alpha_{\text{MP}}$ , the misalignment angle,  $\delta$ , the inclination angle,  $i$ , and the precession rate,  $\Omega_{\text{p}}$ . The phase of the inflection point of the RVM under the MP,  $\phi_{0_{\text{MP},k}}$  for each epoch  $k$  was also included in the analysis as a free parameter. The geometry of the system is illustrated in Fig 1. We used the Bayesian sampling tool POLYCHORD (22) to explore the parameter space of the model (20). The  $1\text{-}\sigma$  uncertainty intervals were derived from the one-dimensional marginalized posterior distributions (shown in Fig. S3), giving the 68 per cent confidence level on each parameter.

We measure  $\alpha_{\text{MP}} = 99^{\circ}.41 \pm 0^{\circ}.17$  (and therefore  $\alpha_{\text{IP}} = 180^{\circ} - \alpha_{\text{MP}} = 80^{\circ}.62 \pm 0^{\circ}.17$ ), which combined with a separation between the MP and IP close to  $180^{\circ}$  confirms that PSR J1906+0746 is an orthogonal rotator and that the MP and IP emissions originate from opposite magnetic poles. The large  $\delta = 104^{\circ} \pm 9^{\circ}$  is consistent with the pulsar having formed in an asymmetric supernova (SN) explosion, producing a tilt of the spin axis of the younger pulsar in the binary pair (17) relative to the pre-SN orbit (3). As the spin vector contribution to the total angular momentum vector is negligible, we also interpret  $\delta$  as the angle between the orbital angular momentum vector and the pulsar spin vector. With  $\delta \sim 104^{\circ}$ , this suggests that the pulsar spin axis lies close to the orbital plane of this binary system.

This analysis independently determines  $\Omega_{\text{p}} = 2.17 \pm 0.11 \text{ deg yr}^{-1}$  and  $i = 45^{\circ} \pm 3^{\circ}$  in addition to the three previously measured PK parameters (17). This allows us to perform two additional self-consistent tests of GR in this system (see Fig. 2). Both values agree with the GR predictions within  $1\sigma$ . The constraint on  $\Omega_{\text{p}}$  tests GR at a 5% uncertainty level, tighter than the precession rate measurement in the Double Pulsar system (18). The parametrization of our model allows us to determine  $i$  without ambiguity, in contrast to information obtained solely from pulsar timing where only  $\sin i$  can be derived.

From our fitted model, we can describe the evolution of the impact parameters for both the MP and IP,  $\beta_{\text{MP}}(t)$  and  $\beta_{\text{IP}}(t)$  (see Fig. S4) and the latitudinal extent of the pulsar beam (i.e. the

largest value of  $|\beta|$  for which emission is observed). Our model predicts that in 1998  $\beta_{\text{MP}} \sim 5^\circ$  and  $\beta_{\text{IP}} > 22^\circ$ , coinciding with the strong detection of the MP and the non-detection of the IP in the PMPS data (15). The appearance of the IP between 1998 and 2004 corresponds to  $\beta_{\text{IP}}(2001) \sim +20^\circ$ . By 2018, our LOS to the IP had traversed to  $\beta_{\text{IP}}(2018) \sim -6^\circ$  so we infer a latitudinal extent for the IP of  $\sim 20^\circ$ . For the MP, we are only able to map the Southern part of the emission beam,  $-5^\circ < \beta_{\text{MP}} \lesssim -22^\circ$ , after which the emission is no longer detected. The appearance of the IP and the disappearance of the MP at the same  $|\beta|$ , suggests that the MP and IP share the same latitudinal extent of  $\sim 22^\circ$ . We therefore predict that the IP will disappear from our LOS around 2028 to reappear between 2070 to 2090 (Fig. S4). The MP should reappear around 2085–2105.

With our determination of the geometry of the system, we can use the observed pulse profiles recorded at different epochs, including the reprocessed PMPS data (20), to reconstruct (20) the sky-projected beam maps of the radio emission from both magnetic poles (Fig. 3) and its polarisation properties (Fig. 4). Previous attempts at mapping the pulsar emission have been published for other pulsars, e.g. (23). Such plots must not be viewed as strict maps of active fieldlines anchored on the polar cap, but rather as projections of the emission on the sky.

The map shows emission from both sides of the IP magnetic pole, ruling out models predicting that radio emission is restricted to one side of the pole (e.g. (24)). The IP emission pattern is not symmetric in the latitudinal direction or with the MP. The IP weakens when our LOS crosses the magnetic pole. This finding matches theoretical predictions of the current density in the polar cap in case of an orthogonal rotator, albeit at low radio emission height (25, 26). Radio emission is produced at a height above the pulsar where any higher-order magnetic field components should have diminished. In a standard scenario where emission is produced in the entire open field-line region, we would expect the radio beam to be circular. Yet the observed beam is elongated and smaller in the longitudinal direction than expected (Fig. 3).

The passage of the LOS over the IP magnetic pole coincides with a drop in fractional linear polarisation. At the same time, the circular polarisation (Stokes V) appears to change sign when crossing the magnetic pole (Fig. 4 and S5) (20). The fractional linear polarisation of the MP decreases as our LOS moves away from the centre of the MP beam while some unpolarised pulse components are shown to appear and disappear on timescales of months (20).

If we assume that the emission region is symmetric around the magnetic meridian and that the radiation is beamed in the forward direction of the relativistic charge flow along the magnetic field lines, then the rotation of the pulsar magnetosphere in the observer frame causes the pulse profile to precede the magnetic meridian and the PA to lag it.

Models predict that the total phase shift  $\Delta\phi_S$  between the midpoint of the pulse profile and the inflection point of the PA swing is given by  $\Delta\phi_S \approx 4h_{\text{em}}/R_{\text{LC}}$ , where  $h_{\text{em}}$  is the emission height and the light cylinder radius  $R_{\text{LC}} = cP_S/2\pi$ , with  $c$  being the speed of light (11, 12). This relationship is expected to be valid for small emission heights,  $h_{\text{em}} \lesssim 0.1R_{\text{LC}}$ . But these models predict different contributions to the aforementioned shifts in the pulse profile and the PA curve. There is also a shift of the PA in absolute value but this can be neglected here as  $\alpha \sim 90^\circ$  (27).

Measuring the phase shifts  $\Delta\phi_{\text{SMP},k}$  for the MP at a given epoch  $k$  (and its impact parameter,  $\beta(k)$ ), gives an estimate of the MP emission heights  $h_{\text{emMP},k}$ , assuming all shifts are due to rotational effects. The emission heights for the IP,  $h_{\text{emIP},k}$ , can be derived in the same way, also using the RVM inflection points for the IP given by  $\phi_{0\text{IP},k} = \phi_{0\text{MP},k} + 180^\circ$ . These results show that the emission heights range from close to the surface of the pulsar for low impact parameter  $\beta$  (when our LOS is atop of the magnetic pole), to about 320 km for large  $\beta$ , matching the theoretical prediction (28) (Fig. 5), even though this theoretical prediction only depends on  $\alpha$  and  $\beta$ . Deviations are observed for LOSs close to the beam edge of the MP, and large  $\beta$  for the IP, where we may observe a different active patch of the IP beam as suggested by the polarisation properties (e.g. the sign of Stokes V under the IP has flipped between 2009 and

2012, see Fig. 4 and Fig. S5).

The latitudinal extent of a pulsar beam determines the pulsar beaming fraction (i.e. the portion of sky illuminated by the pulsar beam). This parameter affects the predicted number of Galactic double neutron stars (DNSs) population and, hence, the expected gravitational wave detection rate for neutron star mergers (29). Usually the latitudinal extent of the beam cannot be independently determined and so the expected beam radius  $\rho$  for a conal emission beam is used. This beam shape is usually expected, although its internal structure and/or filling factor is still a matter of debate (10). Based on beam cuts given by pulsar profiles, various studies (e.g. (30)) have suggested  $\rho \sim 6.5^\circ P_S^{-0.5}$ , where the dependence on  $P_S$  is consistent with the expectation for dipolar field lines.

Previous studies that estimate the DNS population number and merger rate (29) from a sample of pulsars dominated by only two pulsars (i.e. PSRs J0737–3039A and J1906+0746) have assumed for PSR J1906+0746 an uniform radio luminosity across a conal beam of  $\rho \sim 17^\circ$ . This value is smaller than our observed latitudinal extent of  $22^\circ$  that combined with  $\alpha_{MP} = 99^\circ.4$ , gives a large beaming fraction of 0.52 but with substantial luminosity variations. The simple conal beam model with uniform luminosity can not be used for PSR J1906+0746 to reliably constrain the DNS merger rate.

## References and Notes

1. T. Damour, R. Ruffini, *C. R. Acad. Sci. Paris, Serie A - Sciences Mathematiques* **279**, 971 (1974).
2. N. Wex, V. Kalogera, M. Kramer, *Astrophys. J.* **528**, 401 (2000).
3. H.-T. Janka, *Astrophys. J.* **837**, 84 (2017).
4. J. M. Weisberg, R. W. Romani, J. H. Taylor, *Astrophys. J.* **347**, 1030 (1989).



5. M. Kramer, *Astrophys. J.* **509**, 856 (1998).
6. T. Damour, J. H. Taylor, *Phys. Rev. D* **45**, 1840 (1992).
7. I. H. Stairs, S. E. Thorsett, Z. Arzoumanian, *Phys. Rev. Lett.* **93**, 141101 (2004).
8. V. Radhakrishnan, D. J. Cooke, *Astrophys. Lett.* **3**, 225 (1969).
9. M. M. Komesaroff, *Nature* **225**, 612 (1970).
10. D. R. Lorimer, M. Kramer, *Handbook of Pulsar Astronomy* (Cambridge University Press, 2005).
11. M. Blaskiewicz, J. M. Cordes, I. Wasserman, *Astrophys. J.* **370**, 643 (1991).
12. J. Dyks, *Mon. Not. R. Astron. Soc.* **391**, 859 (2008).
13. M. Kramer, S. Johnston, *Mon. Not. R. Astron. Soc.* **390**, 87 (2008).
14. J. Arendt, P. N., J. A. Eilek, *ArXiv e-prints* pp. astro-ph/9801257 (1998).
15. D. R. Lorimer, *et al.*, *Astrophys. J.* **640**, 428 (2006).
16. R. N. Manchester, *et al.*, *Mon. Not. R. Astron. Soc.* **328**, 17 (2001).
17. J. van Leeuwen, *et al.*, *Astrophys. J.* **798**, 118 (2015).
18. R. P. Breton, *et al.*, *Science* **321**, 104 (2008).
19. E. Fonseca, I. H. Stairs, S. E. Thorsett, *Astrophys. J.* **787**, 82 (2014).
20. Materials and methods are available as supplementary materials.
21. M. Kramer, N. Wex, *Classical and Quantum Gravity* **26**, 073001 (2009).

22. W. J. Handley, M. P. Hobson, A. N. Lasenby, *Mon. Not. R. Astron. Soc.* **453**, 4384 (2015).
23. R. N. Manchester, *et al.*, *Astrophys. J.* **710**, 1694 (2010).
24. J. Arons, *Astrophys. J.* **266**, 215 (1983).
25. A. N. Timokhin, J. Arons, *Mon. Not. R. Astron. Soc.* **429**, 20 (2013).
26. S. E. Gralla, A. Lupasca, A. Philippov, *Astrophys. J.* **851**, 137 (2017).
27. J. A. Hibschan, J. Arons, *Astrophys. J.* **546**, 382 (2001).
28. R. Yuen, D. B. Melrose, *Publ. Astron. Soc. Aus.* **31**, e039 (2014).
29. R. O'Shaughnessy, C. Kim, *Astrophys. J.* **715**, 230 (2010).
30. M. Kramer, R. Wielebinski, A. Jessner, J. A. Gil, J. H. Seiradakis, *Astron. Astrophys. Suppl. Ser.* **107**, 515 (1994).
31. W. van Straten, *Astrophys. J. Suppl. Ser.* **204**, 13 (2013).
32. C. G. Bassa, *et al.*, *Mon. Not. R. Astron. Soc.* **456**, 2196 (2016).
33. R. C. Jones, *J. Opt. Soc. Am.* **31**, 488 (1941).
34. W. M. Yan, *et al.*, *Mon. Not. R. Astron. Soc.* **414**, 2087 (2011).
35. L. Kasian, Radio observations of two binary pulsars, Ph.D. thesis, University of British Columbia (2012).
36. S. M. Ransom, New search techniques for binary pulsars, Ph.D. thesis, Harvard University (2001).

37. W. van Straten, P. Demorest, S. Osłowski, *Astronomical Research and Technology* **9**, 237 (2012).
38. G. Desvignes, modelRVM, <http://dx.doi.org/10.5281/zenodo.3265755> (2019).
39. R. Brun, F. Rademakers, *Nuclear Instruments and Methods in Physics Research Section A: Accelerators, Spectrometers, Detectors and Associated Equipment* **389**, 81 (1997).
40. F. Feroz, M. P. Hobson, M. Bridges, *Mon. Not. R. Astron. Soc.* **398**, 1601 (2009).
41. C. D. Ilie, S. Johnston, P. Weltevrede, *Mon. Not. R. Astron. Soc.* **483**, 2778 (2019).
42. V. Radhakrishnan, J. M. Rankin, *Astrophys. J.* **352**, 258 (1990).
43. V. S. Beskin, A. A. Philippov, *Mon. Not. R. Astron. Soc.* **425**, 814 (2012).
44. J. Dyks, B. Rudak, *Astrophys. J.* **598**, 1201 (2003).

## Acknowledgments

We thank Norbert Wex and Simon Johnston for useful discussions, Alessandro Ridolfi for sharing the flux calibration observations for PUPPI and the PALFA collaboration for recording some of the early Arecibo observations. We acknowledge the use of the Hercules cluster hosted at the Max Planck Computing and Data Facility in Garching. This research has made extensive use of NASA's Astrophysics Data System. **Funding:** GD and MK gratefully acknowledge support from European Research Council (ERC) Synergy Grant BlackHoleCam Grant Agreement Number 610058. KJL received support from 973 program 2015CB857101, NSFC U15311243, XDB23010200, 11690024, and funding from Max-Planck Partner Group. JvL acknowledges funding from the Netherlands Organisation for Scientific Research (NWO) under project "CleanMachine" (614.001.301) and from the ERC under the European Unions Seventh

Framework Programme (FP/2007-2013) / ERC Grant Agreement n. 617199. Pulsar research at UBC is supported by an NSERC Discovery Grant and by the Canadian Institute for Advanced Research. The Arecibo Observatory is operated by SRI International under a cooperative agreement with the NSF (AST-1100968), and in alliance with Ana G. Méndez-Universidad Metropolitana, and the Universities Space Research Association. The Nançay radio Observatory is operated by the Paris Observatory, associated to the French Centre National de la Recherche Scientifique (CNRS) and to the Université d'Orléans. **Author contributions:** GD and MK led the analysis and the writing of the manuscript. KL and AJ provided theoretical input and analysis. JvL, IS and LK performed the Arecibo observations. IC performed the Nançay observations. All authors commented on the manuscript. **Competing interests:** The authors declare no competing interests. **Data and materials availability:** The Parkes data are publicly available and can be requested at <https://data.csiro.au/dap/home> (scan PM0055\_01341\_21). The Nançay and Arecibo datasets can be downloaded from <https://doi.org/10.5281/zenodo.3358819>. The modelRVM tool is available from <https://doi.org/10.5281/zenodo.3265755>. The output parameters of our modelling are listed in Tables S1 and S2.

## Supplementary Materials:

Materials and Methods

Supplementary Text

Figures S1 to S6

Tables S1 to S2

References (31–44)

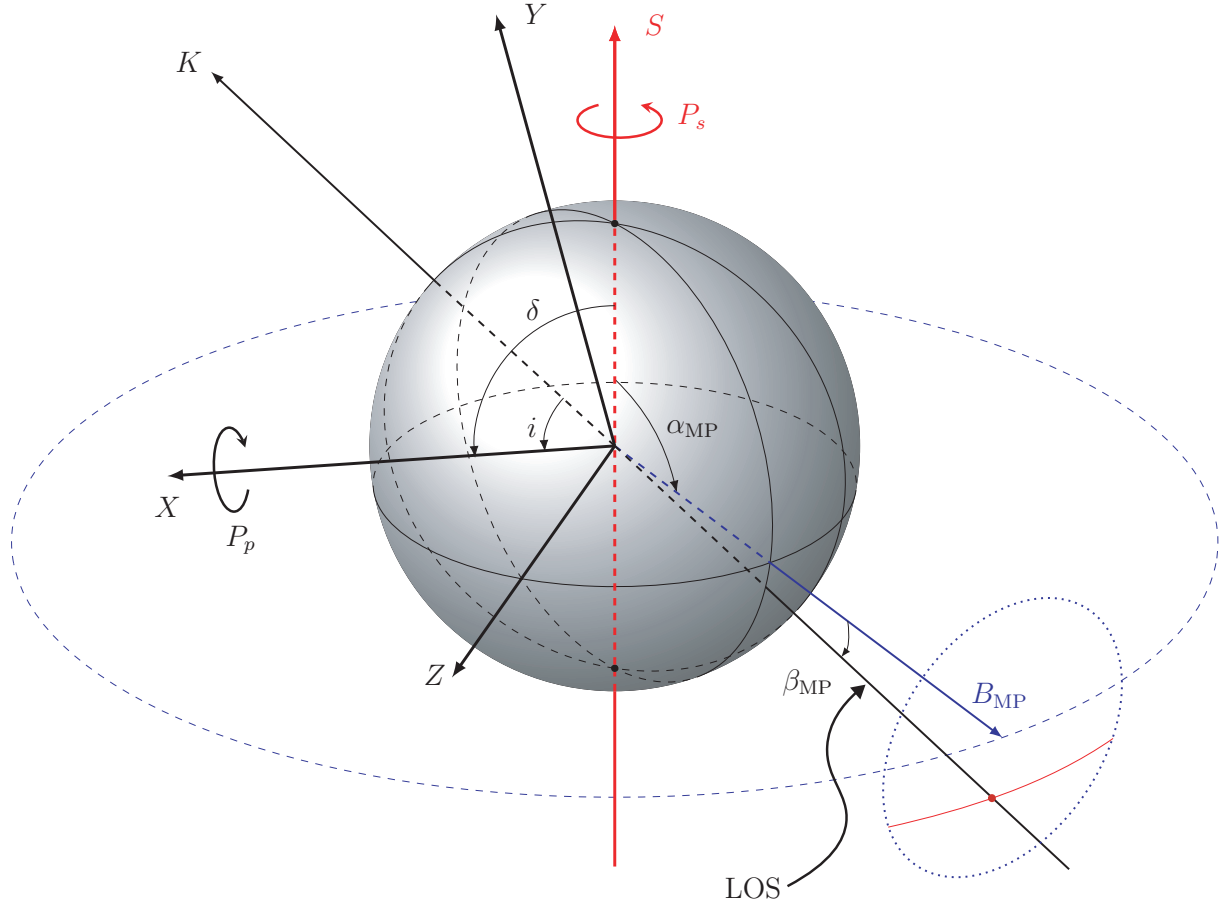


Figure 1: **Geometry of PSR J1906+0746.** The pulsar rotates with a spin period  $P_S = 144$  ms around its spin vector  $S$  shown with the vertical red arrow.  $S$  precesses with a period of  $P_p = 360^\circ/\Omega_p \sim 160$  yr around the total angular momentum vector (misaligned by the angle  $\delta$  from  $S$ ) that can be approximated by the orbital momentum vector  $X$ , perpendicular to the  $Y - Z$  orbital plane.  $i$  is the orbital inclination angle. As the pulsar spins, its magnetic pole corresponding to the MP emission,  $B_{MP}$ , and inclined with an angle  $\alpha_{MP}$  sweeps the sky along the dashed blue trajectory. The MP beam, with the extent pictured by the dotted blue circle, crosses our LOS represented by the  $K$  vector if  $|\beta_{MP}| < 22^\circ$ . This allows us to observe a cut, shown with the red curve, through the MP beam. After half a rotation of the pulsar, our LOS can also potentially cut through the IP beam if  $|\beta_{IP}| < 22^\circ$ . For clarity, only the MP beam is shown.

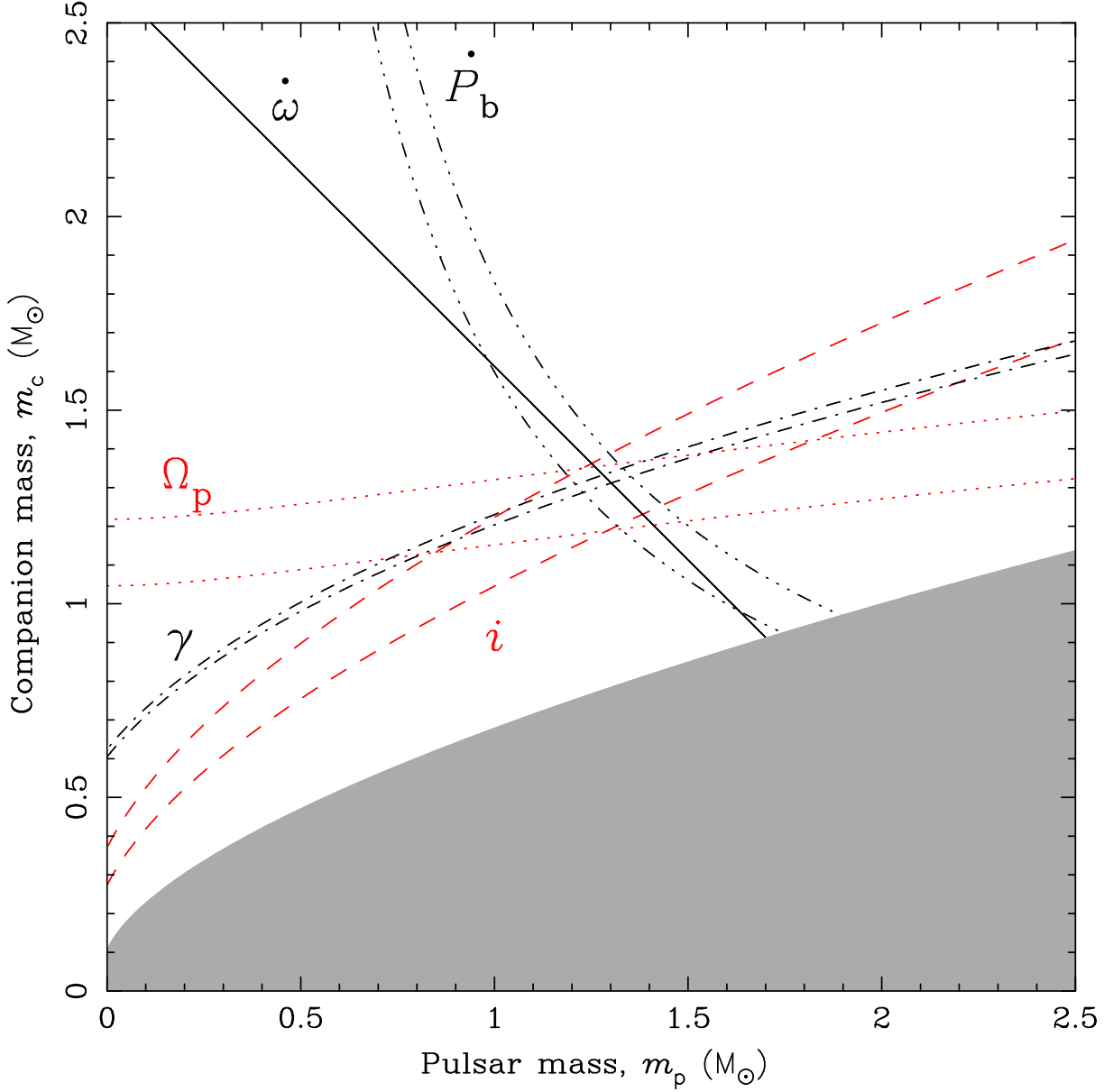


Figure 2: **Mass-mass diagram.** The black lines delimit the  $1-\sigma$  contours from the measurements of the orbital period decay,  $\dot{P}_b$ , the periastron advance,  $\dot{\omega}$ , and the time dilation,  $\gamma$  (17). The red dotted and dashed lines delimit our two additional constraints, the measurements of spin-precession rate  $\Omega_p$  and inclination angle  $i$ , respectively. The grey parameter space is excluded by the mass function due to  $\sin i \leq 1$ . All parameters are consistent with  $m_p = 1.29 \pm 0.01 M_\odot$  and  $m_c = 1.32 \pm 0.01 M_\odot$ .

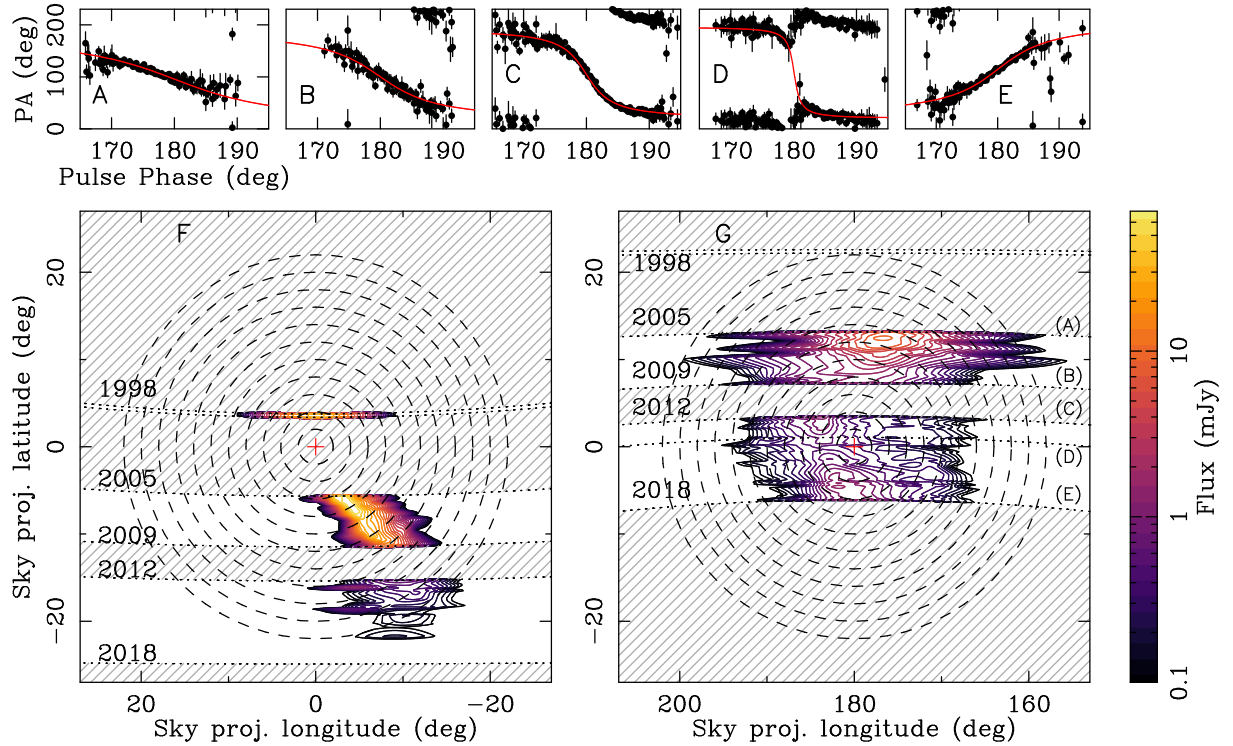


Figure 3: **Beam maps of the radio emission.** Two-dimensional contours of the reconstructed Stokes I emission maps (on a logarithmic color scale), as projected on the sky, for the MP (F) and the IP (G). The reference frame of these maps is fixed on the vertical spin vector  $S$  at longitude zero and  $180^\circ$  pointing towards negative latitude. The red crosses at  $(0,0)$  and  $(180,0)$  indicate the pulsar's magnetic pole on the MP and IP maps, respectively, and the dashed circles show increments of two degrees in the beam map. The dotted lines represent the LOSs at a given year, indicated on the left side. The hatched areas correspond to the parts of the maps that were not observed. (A-E) show the PA measurements (in black) and the fit by the precessional RVM (the red curve) corresponding to the LOSs labelled on the IP map.

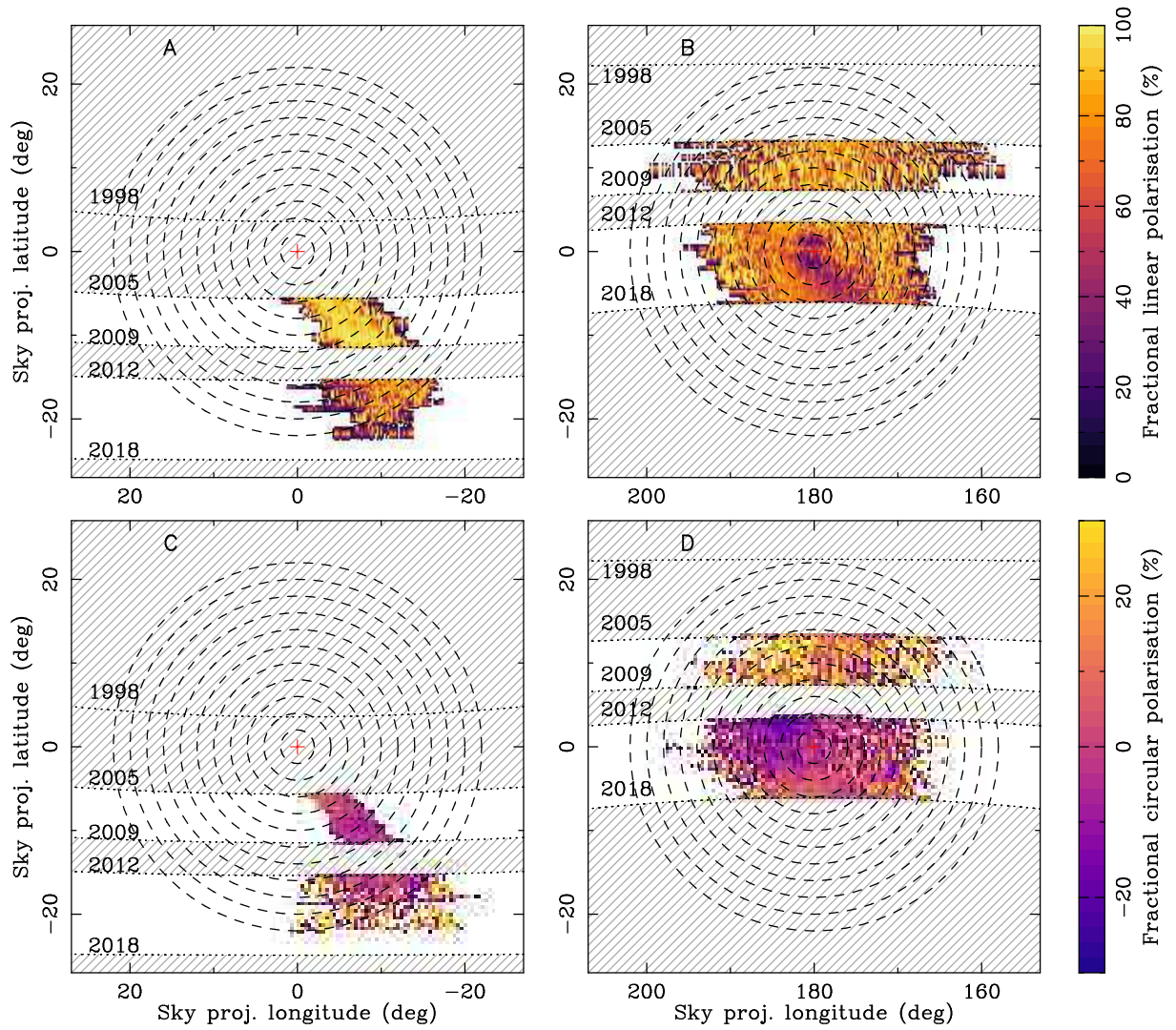


Figure 4: **Polarisation beam maps.** Same as Figure 3F-G, but showing fractional linear polarisation for the MP (A) and IP (B) and fractional circular polarisation for the MP (C) and IP (D).



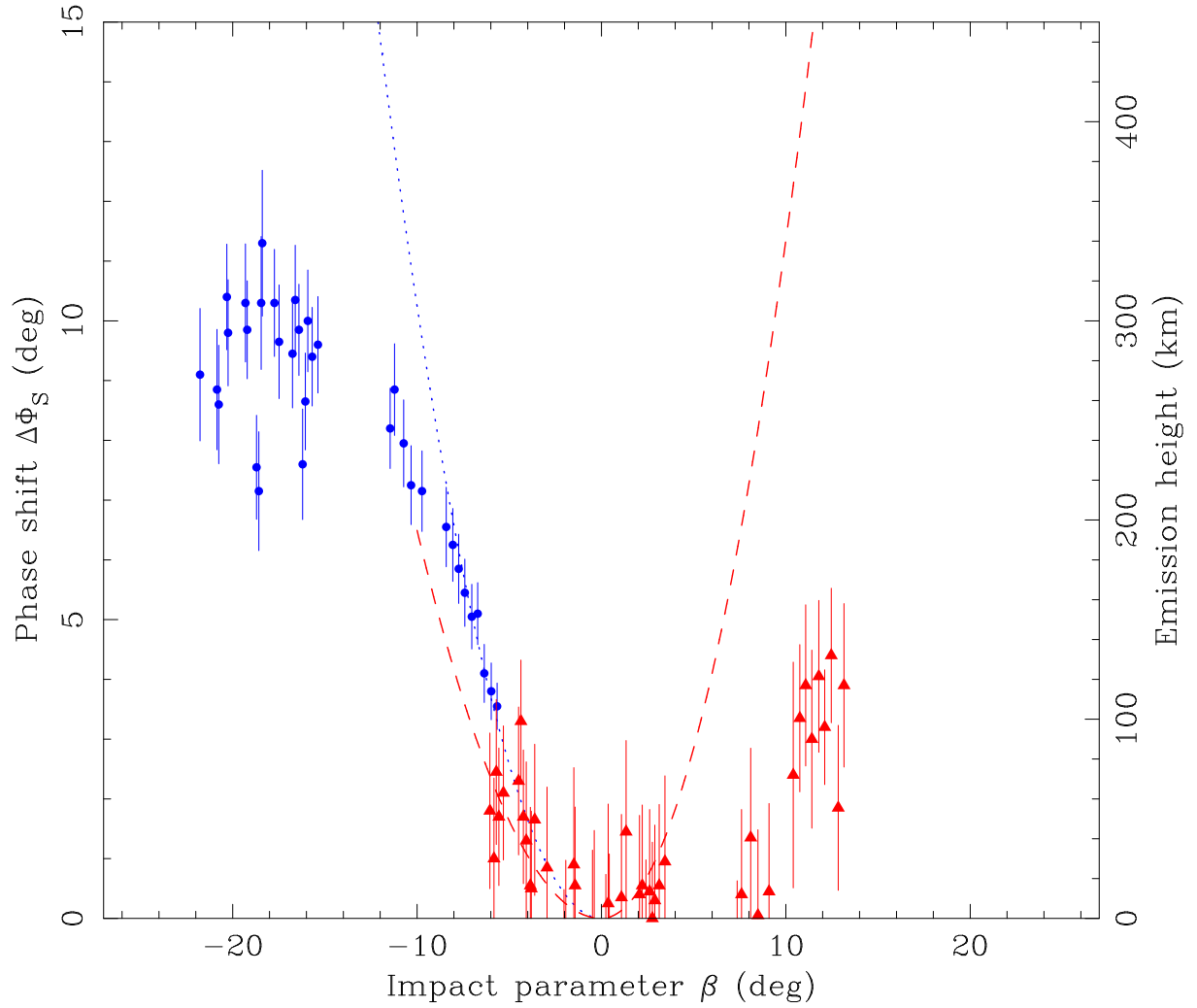


Figure 5: **Radio emission heights.** Phase shift  $\Delta\Phi_S$  of the PA from Stokes I (left axis) with the derived emission height (right axis) for the MP (blue data points) and IP (red data points) as a function of  $\beta$ . The blue and red dashed curves represent the theoretical emission height as a function of  $\beta$ .

## Materials and Methods

**Calibration and post-processing of the data.** PSR J1906+0746 was observed with the Nançay Radio Telescope between 2005 and 2009 with the Berkeley-Orleans-Nançay (BON) backend at a central frequency of 1.4 GHz (17). However, there was at the time no observation of the polarised noise diode along with the pulsar observation that are typically required to calibrate polarisation data.

To calibrate in polarisation the Nançay archival data, we applied a matrix-template matching calibration scheme (31, 32). We construct the Jones matrix (33) by comparing a well-calibrated observation of a reference pulsar to a non-calibrated observation of the same pulsar recorded with the same backend at the same observing frequency.

We choose the millisecond pulsar (MSP) PSR B1937+21 as our reference pulsar due to its well known polarimetric properties (34), large flux density and high observing cadence at 1.4 GHz with the Nançay radio telescope between 2005 and 2009. The reference observation comes from a 2010 observation of this pulsar with the BON backend that has been calibrated with an observation of the noise diode. These reference calibrated observations were found to be consistent with the previously published polarisation results (34).

Each time a change in the instrumental response of the BON backend is detected through visual inspection of the polarisation data of PSR B1937+21 between 2005 and 2009, a new calibrator solution that encompass the observations showing the same polarimetric response is derived. When a reliable calibrator covering a given time span could not be obtained, the corresponding data were discarded from the analysis. A total of 29 calibrator solutions were necessary to cover the five years of BON observations.

As a sanity check, we applied our set of 29 calibrators to the uncalibrated observations of PSR J1909–3744, another regularly observed and bright MSP, recorded with the BON backend

and covering the same time span as PSR J1906+0746. We inspected the polarisation profiles and measured the average PA value under the main pulse to check for any secular variations or artifacts that might have been introduced by our multi-epochs calibrators without finding any systematics other than caused by the diurnal variation of the ionospheric electronic content.

After applying the calibrators to the BON data, we averaged the observations to form a set of pulse profiles each spanning up to three months. As both the observing cadence and the signal-to-noise ratio (S/N) of this pulsar decreased with time, we only made use of 9 averaged profiles spanning June 2005 to July 2007.

PSR J1906+0746 was also observed with Arecibo and the Astronomical Signal Processor (ASP) pulsar backend between May 2006 and August 2009 at a frequency of 1.44 GHz (17, 35). Using observations of the pulsed noise diode, the pulsar B1929+10 and the quasar B1442+101 for flux calibration, we calibrated five high S/N observations spanning May 2008 to August 2009.

Other archival data were discarded because they could not provide calibrated polarisation information or because the S/N of the pulse profiles was too low to contribute to the analysis while increasing the dimensionality of our modelling.

In March 2012, we exploited the then newly available PUPPI backend at the Arecibo radio telescope to resume the monitoring of PSR J1906+0746 at 1.38 GHz, usually observed for 2 hours on a monthly basis. We have 33 calibrated observations spanning March 2012 to June 2018. These new data allow for polarisation and flux calibration of the recorded Stokes profiles through observations of a pulsed noise diode and the quasar PKS 2209+080.

We measured the effect of Faraday rotation on Stokes Q and U of the BON and PUPPI data and found the average rotation measure (RM) to be  $152.3 \pm 0.7 \text{ rad m}^{-2}$ , in agreement with previous results (15). The ASP data were not used to estimate the RM due to their limited bandwidth but all data were corrected for Faraday rotation using the average RM. These observations

are summarized in Table S2.

In addition to the data described above, we reprocessed the PMPS (16) archival data that show a detection of PSR J1906+0746 in 1998 (15). The sky position of PSR J1906+0746 was observed on August 3rd, 1998, i.e. Modified Julian Date (MJD) 51028, at a central frequency of 1374 MHz and recorded in 1-bit search-mode filterbank data. Using PRESTO (36), we dedispersed and folded these time-series data, using the estimated dispersion measure,  $DM = 217 \text{ pc cm}^{-1}$ , and pulse period of the pulsar,  $P_S \sim 144.079 \text{ ms}$ , respectively, to create an average pulse profile. Due to the 3-MHz wide channels used to record the PMPS data, intra-channels dispersion,  $\tau_{DM} \sim 2 \text{ ms}$ , is expected to widen the observed pulse profile that consists of a single component (see Fig S1). This component is assumed to be the MP (15), as later confirmed by our prediction of  $\beta$  in 1998, and we set the midpoint of this component to be at longitude  $0^\circ$ . As the PMPS data only provide Stokes I information, we simply flux calibrated the pulse profile assuming the radiometer equation (see e.g. (10)) and the PMPS parameters (16). The uncertainty of the flux-calibration using the radiometer equation is assumed to be 20%. The PMPS pulse profile is therefore only presented in the Stokes I sky-projected beam maps to constrain the latitudinal extent of the beam emission.

**RVM fitting with MODELRVM** To fit the PA of the linear polarisation to the RVM, we follow the International Astronomical Union convention that measures the PA counter-clockwise on the sky. We also make use of the technique introduced in PSRMODEL as part of the PSRCHIVE package (37) that models the observed linear polarisation  $L$  as a complex quantity,  $L = Q + iU$ , given the measured Stokes parameters  $Q$  and  $U$ . In PSRMODEL, the phase of  $L$ , i.e. the PA  $\Psi$ , is predicted by the RVM while the amplitude of  $L$  is a free parameter. Modelling the complex  $L$  has a number of advantages (37), e.g. the errors on  $Q$  and  $U$  are normally distributed. However, the dimensionality of the modelling increases linearly with the number of data points

included. We derive the complex RVM model that allows us to fix the amplitude of  $L$  instead of setting it free, greatly reducing the dimensionality of the problem. This approach has been introduced in MODEL RVM (38). In MODEL RVM, the estimation of the RVM parameters can be done with traditional  $\chi^2$ -minimization techniques through the MINUIT library from the ROOT data analysis package (39) or using the nested sampling softwares MULTINEST (40) and POLYCHORD (22).

The likelihood  $\Lambda$  of using the  $Q$  and  $U$  data is

$$\log \Lambda = -\frac{1}{2} \sum_{k=1}^{N_{\text{bin}}} \left\{ \frac{[Q_k - \Re(L_k)]^2}{\sigma_{Q_k}^2} + \frac{[U_k - \Im(L_k)]^2}{\sigma_{U_k}^2} \right\} + \text{constant}, \quad (\text{S1})$$

where  $L_k$ ,  $\sigma_{Q_k}$  and  $\sigma_{U_k}$  are the modelled complex linear polarisation intensity and the noise levels of  $Q$  and  $U$  in the  $k$ -th pulsar phase bin, respectively.  $\Re(L_k)$  and  $\Im(L_k)$  are the real and imaginary parts of  $L_k$ , respectively.  $L_k = L_{n,k} e^{2i\Psi_k}$ , where the amplitude  $L_{n,k}$  is a free parameter and  $\Psi_k$  is predicted by the RVM given  $\alpha, \beta$ , the phase of the RVM inflection point  $\phi_0$ , and the PA value at phase  $\phi_0, \psi_0$ .  $N_{\text{bin}}$  is the number of phase bins under the MP and IP that satisfy the criteria  $L > 1.5\sigma_N$ , where  $\sigma_N$  is the standard deviation of the total-intensity off-pulse noise. In total, we have  $2N_{\text{bin}}$  data points and  $N_{\text{bin}} + 4$  model parameters.

Now, in order to reduce the dimensionality of the model and search only for the four parameters of interest, i.e.  $\alpha, \beta, \phi_0$  and  $\psi_0$ , we marginalize over the parameters  $L_i$ , that  $\Lambda' = \int \Lambda dL_k$ , giving

$$\log \Lambda' = -\frac{1}{2} \sum_{k=1}^{N_{\text{bin}}} \left\{ \frac{[Q_k - \Re(L'_k)]^2}{\sigma_{Q_k}^2} + \frac{[U_k - \Im(L'_k)]^2}{\sigma_{U_k}^2} \right\} + \text{constant}. \quad (\text{S2})$$

$L'_k = L'_{n,k} e^{2i\Psi_k}$  and  $L'_{n,k}$  is given by

$$L'_{n,k} = \frac{\frac{Q_k q_k}{\sigma_{Q_k}^2} + \frac{U_k u_k}{\sigma_{U_k}^2}}{\frac{q_k^2}{\sigma_{Q_k}^2} + \frac{u_k^2}{\sigma_{U_k}^2}}, \quad (\text{S3})$$

where  $q_k = \cos 2\Psi_k$  and  $u_k = \sin 2\Psi_k$ .

We used the likelihood  $\Lambda'$  in MODELRVM to estimate for all epochs the four RVM parameters sampled from uniform priors with MULTINEST. The results of  $\beta_{\text{MP}}$  and  $\beta_{\text{IP}}$  derived from the modelling of the RVM using  $\phi_{0,\text{MP}}$  and  $\phi_{0,\text{IP}}$ , respectively, are shown in Table S2.

**Precessional RVM** As previously discussed in the literature, we expect the absolute PA value of PSR J1906+0746 to change as a function of time due to the precession of its spin axis around the total angular momentum vector (6, 21). To model this effect in the ‘precessional RVM’, we combined the likelihood  $\Lambda'$  from Equation S2 with the equations 2 to 9 from (21).

The required parameters are  $\alpha_{\text{MP}}$ ,  $\delta$ , a reference precessional phase  $\Phi_0$  and a reference PA  $\Delta\psi_0$  at an epoch  $T_0$ , chosen in MODELRVM to be the epoch of the first observation in the dataset,  $T_0 = \text{MJD } 53571$ . For each epoch  $k$ , the phase of the inflection point of the RVM under the MP,  $\phi_{0,\text{MP},k}$  is also a parameter in the model. The inclination angle  $i$  and the precession rate  $\Omega_p$  can either be fixed to the GR values or included as free parameter in the model. The parameters of the model are summarised in Table S1.

As small deviations from the RVM are observed for regions where we expect our line of sight to be extremely close to the magnetic pole, we excluded from our analysis a phase range of  $\sim 3^\circ$  atop of the pole for the 8 epochs recorded between MJD 56500 and 57000. As these phase ranges also correspond to dips in the observed linear polarisation, we performed a phase-resolved RM analysis on these data (averaged over  $\sim 0.35^\circ$  of pulse phase) to check for potential pulsar magnetospheric effects on the polarisation (see e.g. (41)). However no trend were observed within our uncertainties of order 10-20  $\text{rad m}^{-2}$ .

To account for possible variations in the RM coming from e.g. ionospheric electron content that can shift the absolute PA value, we created 2000 data sets where each individual epoch was corrected for an RM drawn from a normal distribution of width  $1.0 \text{ rad m}^{-2}$  and centred at  $152.3 \text{ rad m}^{-2}$ . Then, for each of the 2000 data sets, we used POLYCHORD within MODELRVM

to explore the parameter space of the model with 500 live points, sampled from uniform priors. We equally summed the posterior distributions of each parameter from the 2000 data sets to form the final posteriors (Figure S3).

**Reconstructing the beam map** We begin the beam reconstruction by phase aligning all pulse profiles with respect to  $\phi_{0_{\text{MP},k}}$ , the inflection point of the RVM under the MP, to the same phase of  $0^\circ$ . Consequently, the RVM inflection point for the IP is set at the phase of  $180^\circ$ . In the case of the PMPS data, we interpret the only observed component as the MP and therefore arbitrarily set the midpoint of the pulse to phase  $0^\circ$ . We then fit a set of Gaussian functions to the Stokes I profiles of the MP and IP separately to form noise-free pulse profiles. Finally, we separately perform a two-dimensional spline fit (over time and pulse phase) to the MP and IP noise-free profiles that we map to the sky-projected beam grid given the predicted line of sight. The reference frame of the grid is fixed with respect to the spin vector  $S$ , vertically aligned on phase (also labelled longitude on the maps)  $0^\circ$  and  $180^\circ$ , pointing towards negative latitude. In the maps, at longitude  $0^\circ$  and  $180^\circ$ , the latitude is equivalent to  $\beta_{\text{MP}}$  and  $\beta_{\text{IP}}$ , respectively. We applied the same two dimensional spline fit to reconstruct the beam maps for the linear and circular polarisation, but directly on the linear polarisation  $L$  and circular polarisation  $V$ .

Because the PMPS data partially suffer from dispersion by the interstellar medium, the MP emission from the 1998 LOS represented in the Stokes I emission map (panel (F) in Fig. 3) is slightly broadened compared to its intrinsic width. For clarity, the vertical extent of the 1998 observation, represented by the gap between the two dotted curves, has been exaggerated.

## Supplementary Text

**Polarisation of the beam** Stokes V and the gradient of the PA are shown to flip sign as our LOS crosses the IP magnetic pole (Fig. S2 and S5). A correlation between PA and a change of

sign in Stokes V at the pulse profile midpoint has previously been deduced from a set of pulsars with single LOS observations (42) and matches theoretical predictions (43).

**Caustic emission** Twisted magnetospheres can cause “caustics” from the superposition of emission originating at different locations in the (e.g. outer) magnetosphere, as commonly proposed to explain the shape of light-curves from  $\gamma$ -ray pulsars (e.g. (14)). At radio frequencies such caustics should be depolarised (44), and we speculate that they may be responsible for the strong, unpolarised pulse component trailing the MP that appeared and disappeared very rapidly on two occasions (around September 2012, MJD  $\sim 56200$ ,  $\beta_{\text{MP}} \sim -16^\circ$ , and May 2014, MJD  $\sim 56800$ ,  $\beta_{\text{MP}} \sim -18.5^\circ$ ; see Fig S2).

**Changes in relative emission height between the MP and IP** In practice, it is difficult to distinguish between a tilted beam shape and a gradual shift in phase  $\Delta\phi_S$  due to changing emission heights as a function of  $\beta$ . A change in relative emission height between the MP and IP, and hence, relative phase shift, would partly explain the measured change in separation between the midpoint of the MP and IP pulse profiles,  $\Delta\Phi_I$ , also shown in Fig. S6. If the emission height differs for the MP and IP at a given epoch, the difference in the respective PA shifts due to corotational effects implies that the assumption  $\phi_{0\text{IP},k} = \phi_{0\text{MP},k} + 180^\circ$  is no longer valid and, therefore, that a single RVM does not describe the data optimally. Hence, we also included in the precessional RVM analysis a phase offset  $\Delta\Phi_{\text{RVM}}$  in the RVM curve between the MP and IP, to allow  $\phi_{0\text{IP},k}$  and  $\phi_{0\text{MP},k}$  to vary independently from each other when the emission from both the MP and IP was detected. We find  $\Delta\Phi_{\text{RVM}}$  is consistent with  $0^\circ$  within  $2\sigma$  for all epochs (Fig. S6). While this confirms the validity of our RVM model, the only self-consistent description appears to be that any corotational phase shift mostly impacts on the pulse profile and not on the PA swing.



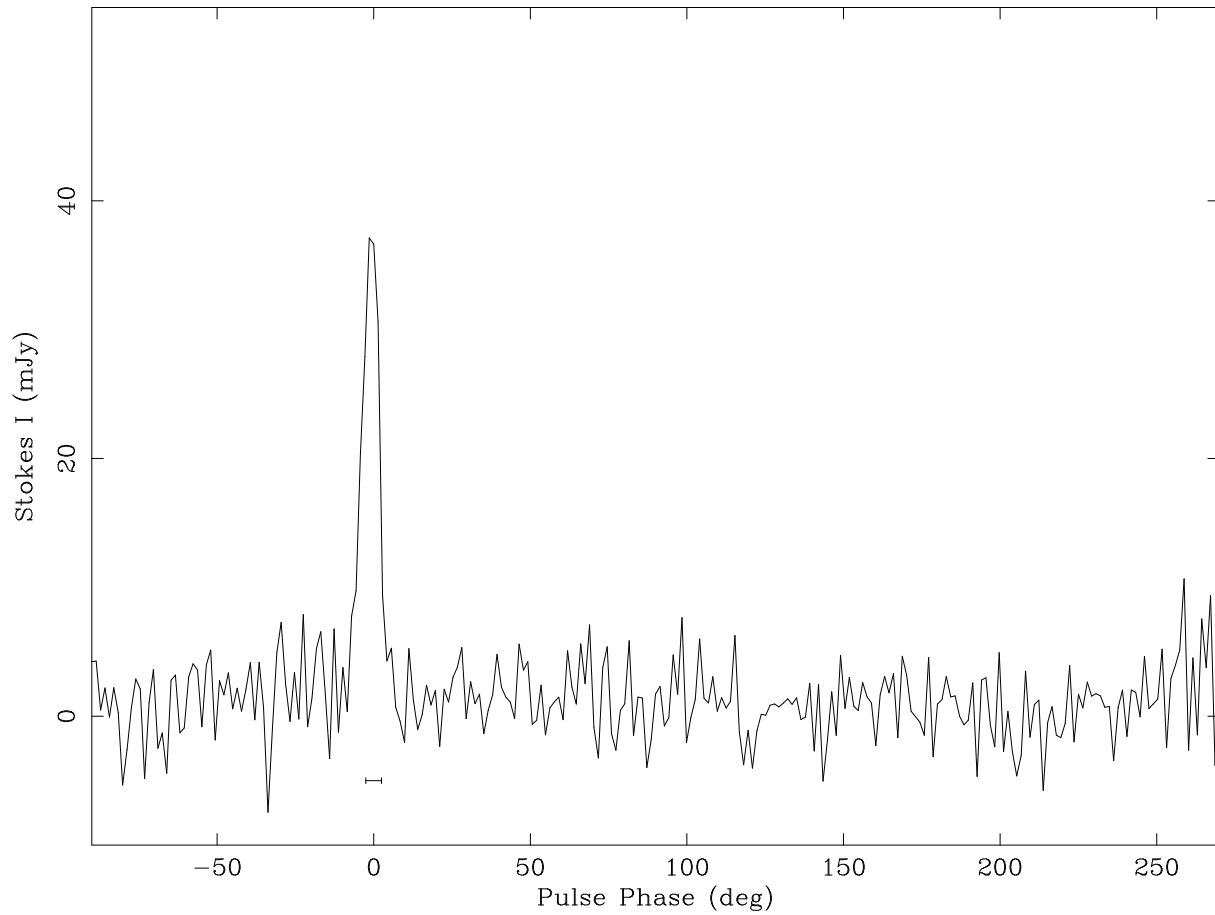


Figure S1: **Archival pulse profile from 1998.** Pulse profile of PSR J1906+0746 from the PMPS archival data as observed on August 3rd, 1998. The scaling of the Stokes I in mJy has been done under the assumption of the radiometer equation and the PMPS parameters (see text). The horizontal error bar under the pulse shows the dispersion broadening of the pulse due to the finite channel bandwidth of the PMPS data.

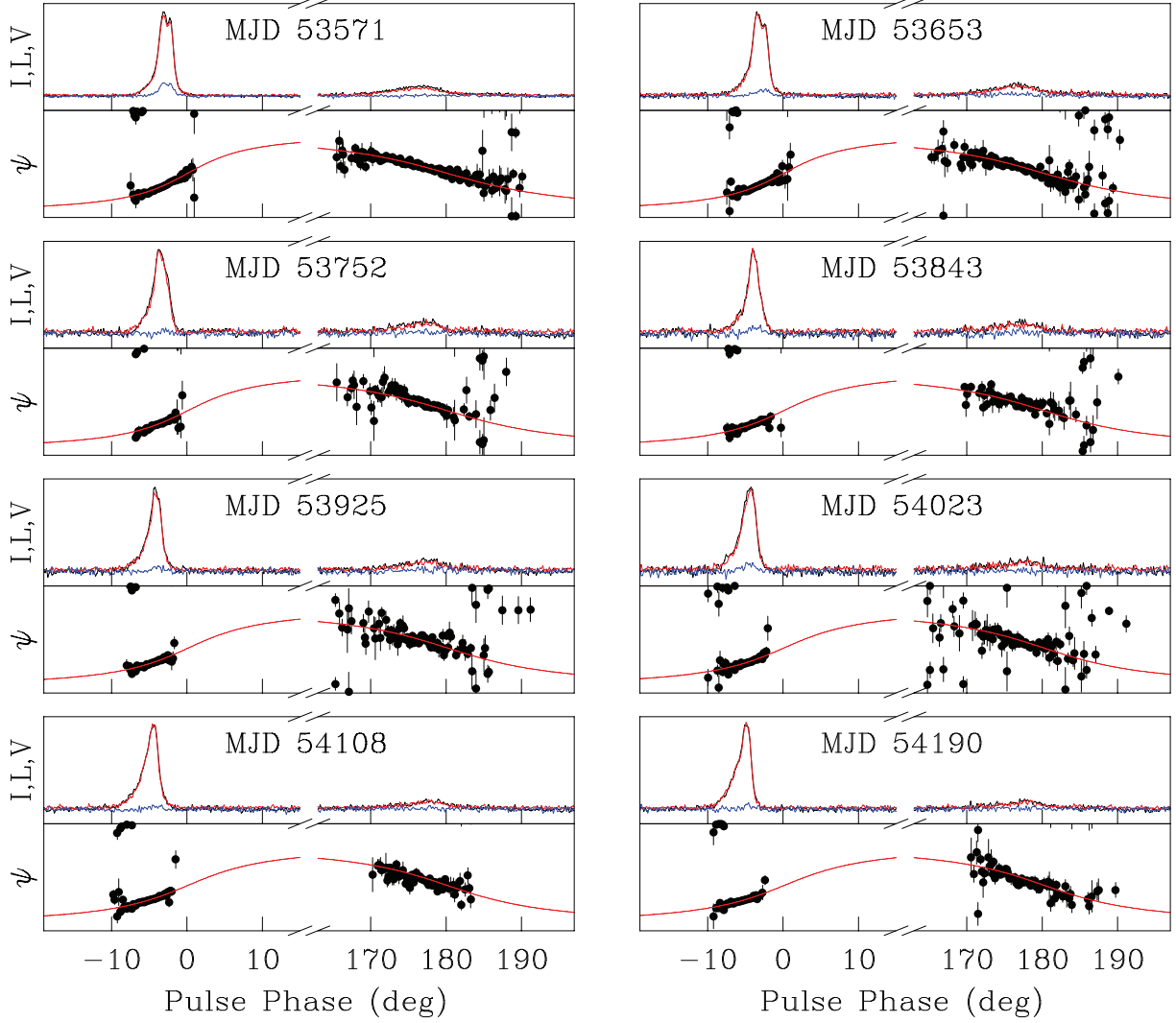


Figure S2: **Polarisation profiles of PSR J1906+0746.** Normalized polarisation profiles and PA measurements of PSR J1906+0746. To improve readability, only the phase around the MP ( $\phi_{0\text{MP}}$  at phase  $0^\circ$ ) and IP ( $\phi_{0\text{IP}}$  at phase  $180^\circ$ ) is displayed. For each epoch, the normalized total intensity profile  $I$ , the linear polarisation  $L$  and the circular polarisation  $V$  are shown in the upper panel in black, red and blue colours, respectively. In the lower panel with the y-axis ranging from 0 to  $230^\circ$ , the black data points represent the PA  $\psi$  of the linear polarisation and the red curve shows the predicted RVM curve from the maximum likelihood value of our precessional RVM model. For the 8 profiles between MJD 56500 and 57000, the  $3^\circ$ -phase ranges atop the IP magnetic pole and corresponding to grey PA values were excluded from the fit. The PA wraps every  $180^\circ$ . The MJD of the averaged profiles are written in the upper panels.

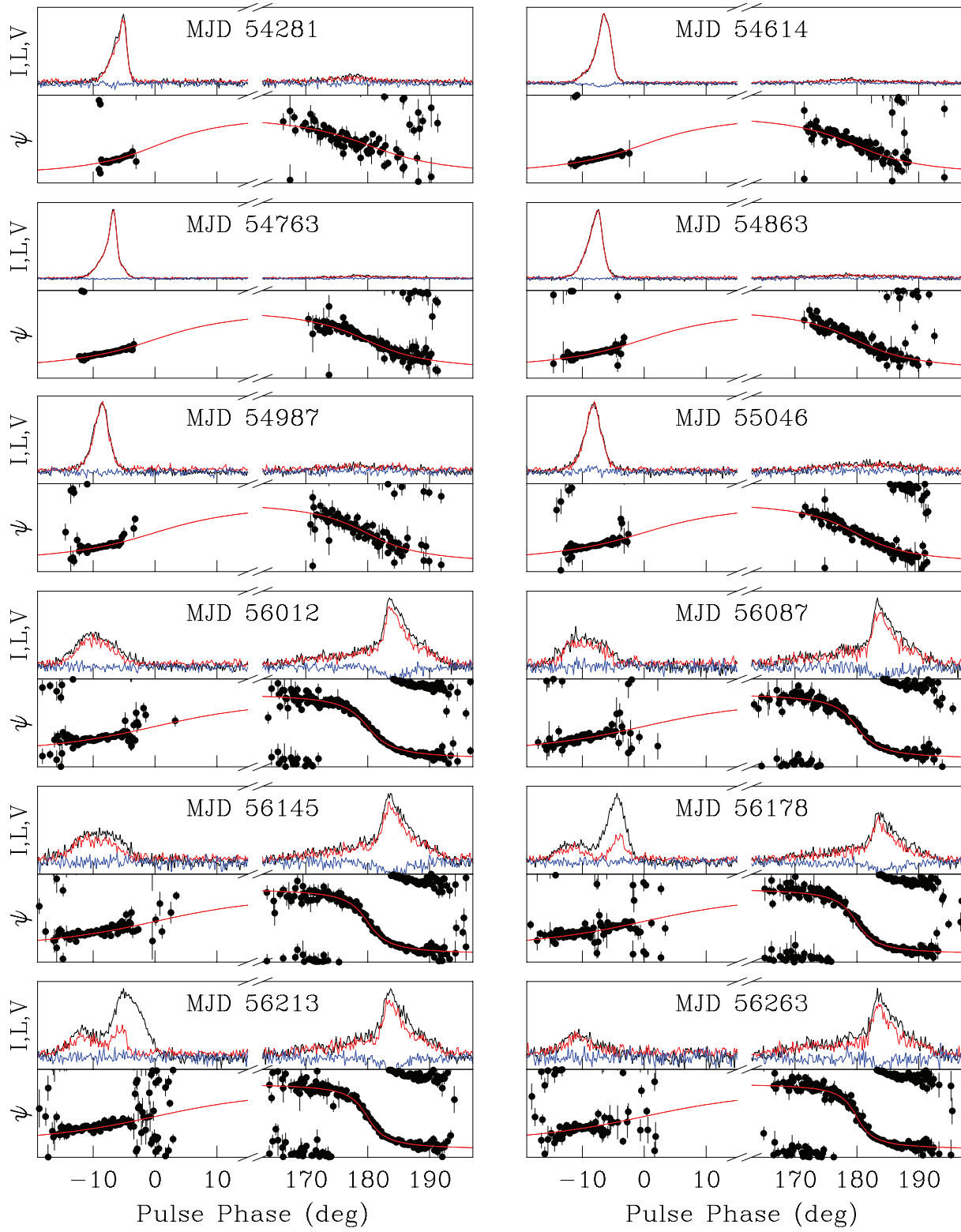


Figure S2: Continued

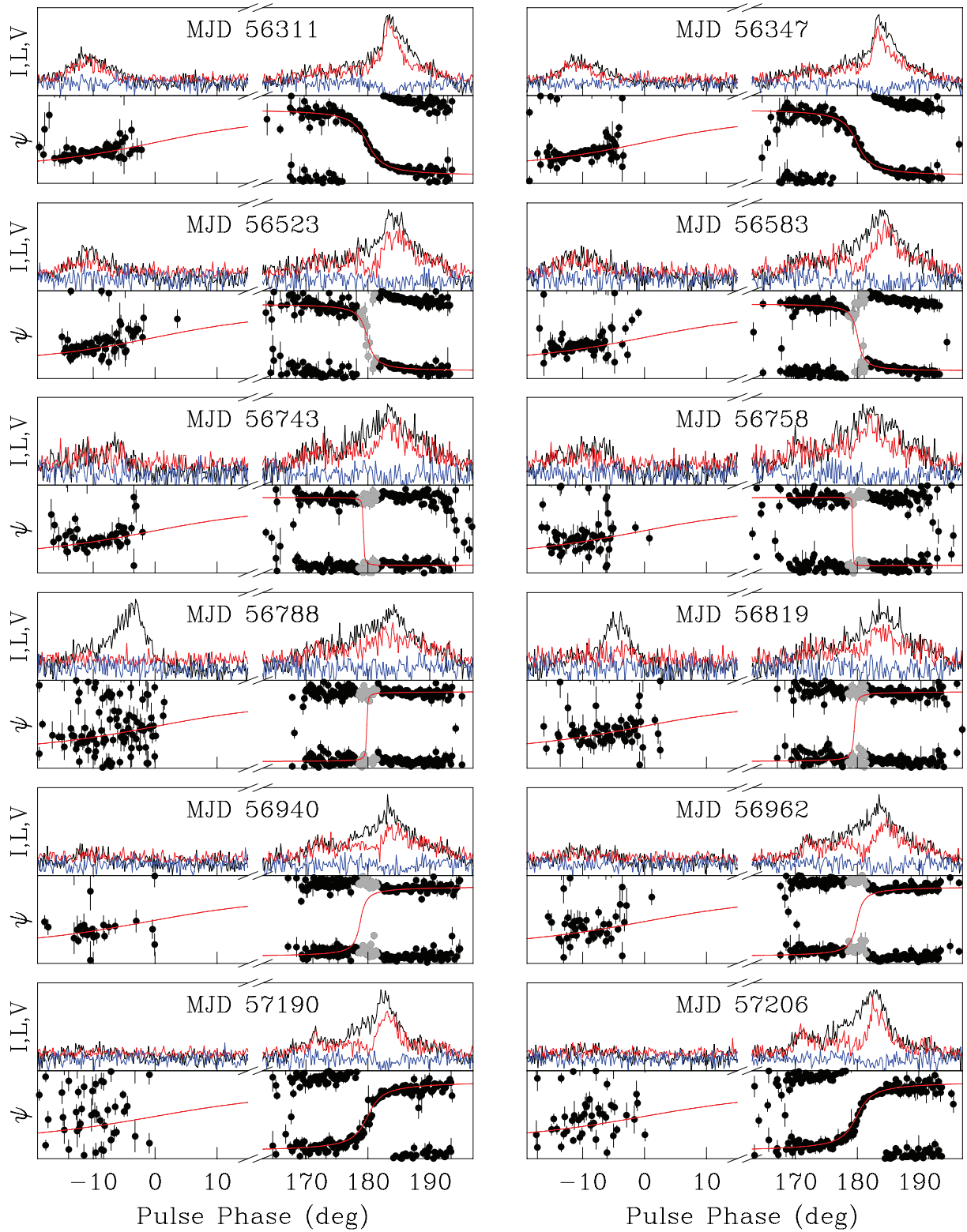


Figure S2: Continued

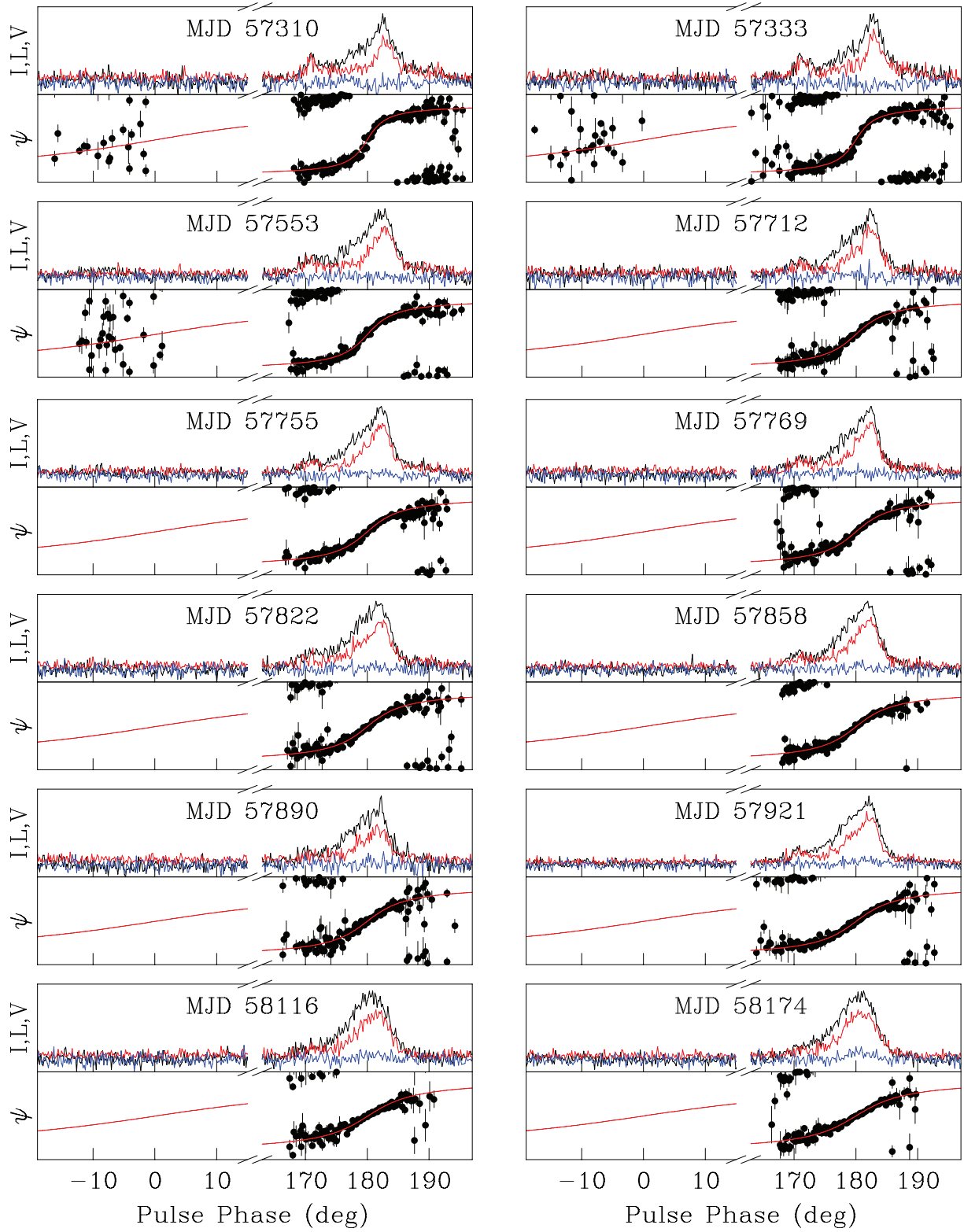


Figure S2: Continued  
12

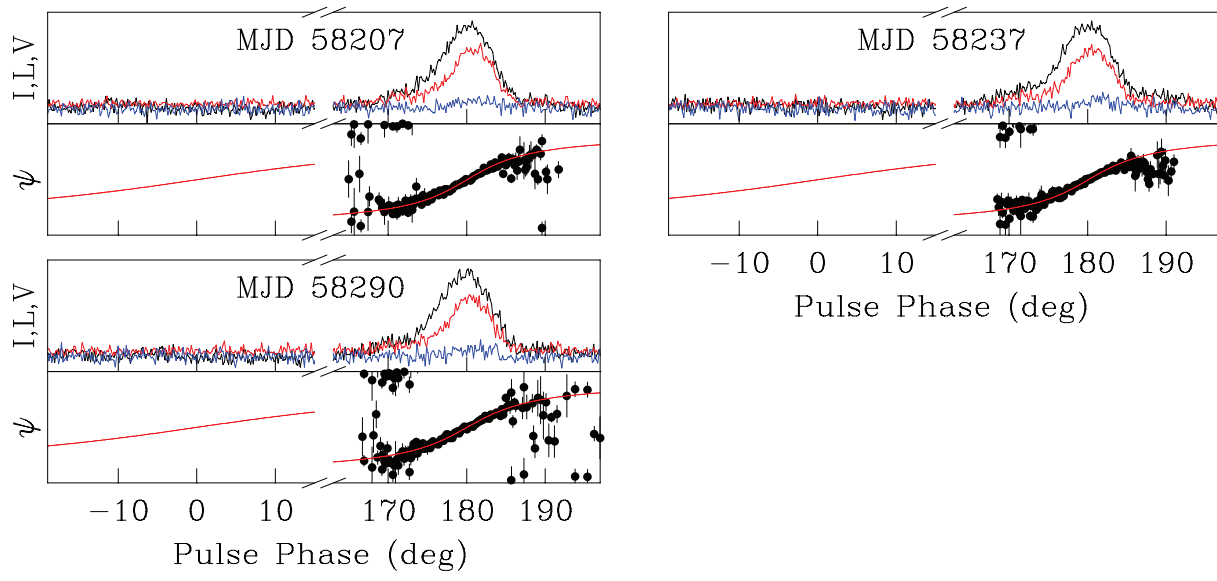


Figure S2: Concluded

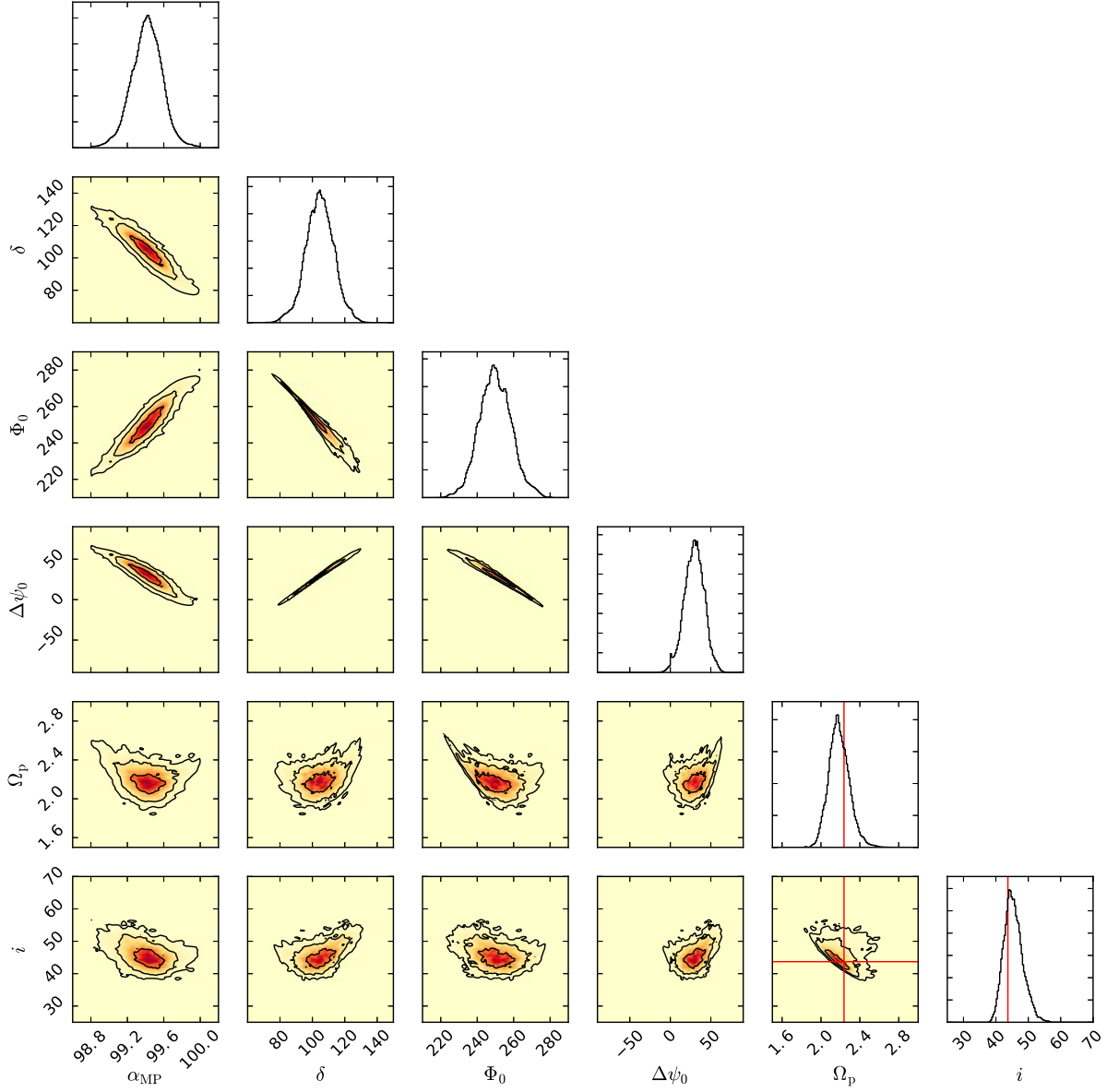


Figure S3: **Posterior probability distributions of the precessional RVM.** One and two-dimensional marginalized posterior probability distributions showing the covariance between the main parameters of interest in the precessional RVM. From top to bottom and left to right, the represented parameters are the angle between the rotation axis and the magnetic axis of the MP,  $\alpha_{\text{MP}}$ , the misalignment angle,  $\delta$ , the reference precessional phase,  $\Phi_0$ , the absolute PA,  $\Delta\psi_0$ , the precession rate,  $\Omega_p$ , and the inclination angle  $i$ . The red lines show the predicted GR values for  $\Omega_p$  and  $i$ , in agreement with our results.

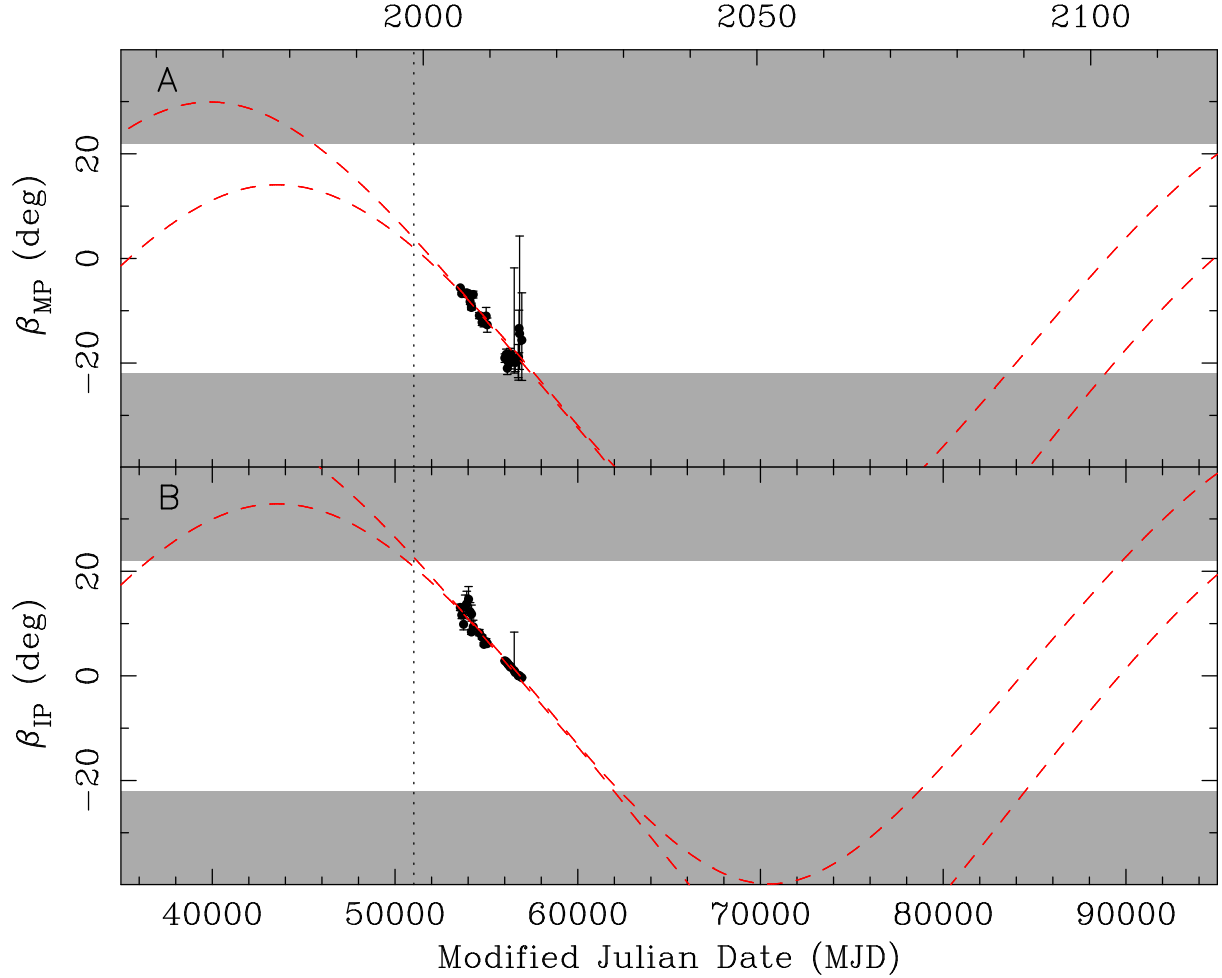


Figure S4: **Evolution of the impact parameter as a function of time.** (A) and (B) show the secular evolution of  $\beta_{\text{MP}}$  and  $\beta_{\text{IP}}$ , respectively, covering the precession period of the pulsar. The data points and error bars are taken from the traditional RVM analysis of each epoch separately. The red dashed curve delimits the 68 per cent confidence levels on  $\beta$  as derived from the posterior results. The grey areas shows the range of impact parameter,  $|\beta| > 22^\circ$ , where the radio emission is assumed not to be detectable based on the observed latitudinal extent of the MP beam. The vertical dotted line indicates  $\text{MJD} = 51028$ , the epoch of the first detection of PSR J1906+0746 in the PMPS archival data. At the time of the first PMPS detection, our model predicts that  $\beta_{\text{MP}} \sim 5^\circ$  and  $\beta_{\text{IP}} > 22^\circ$ .



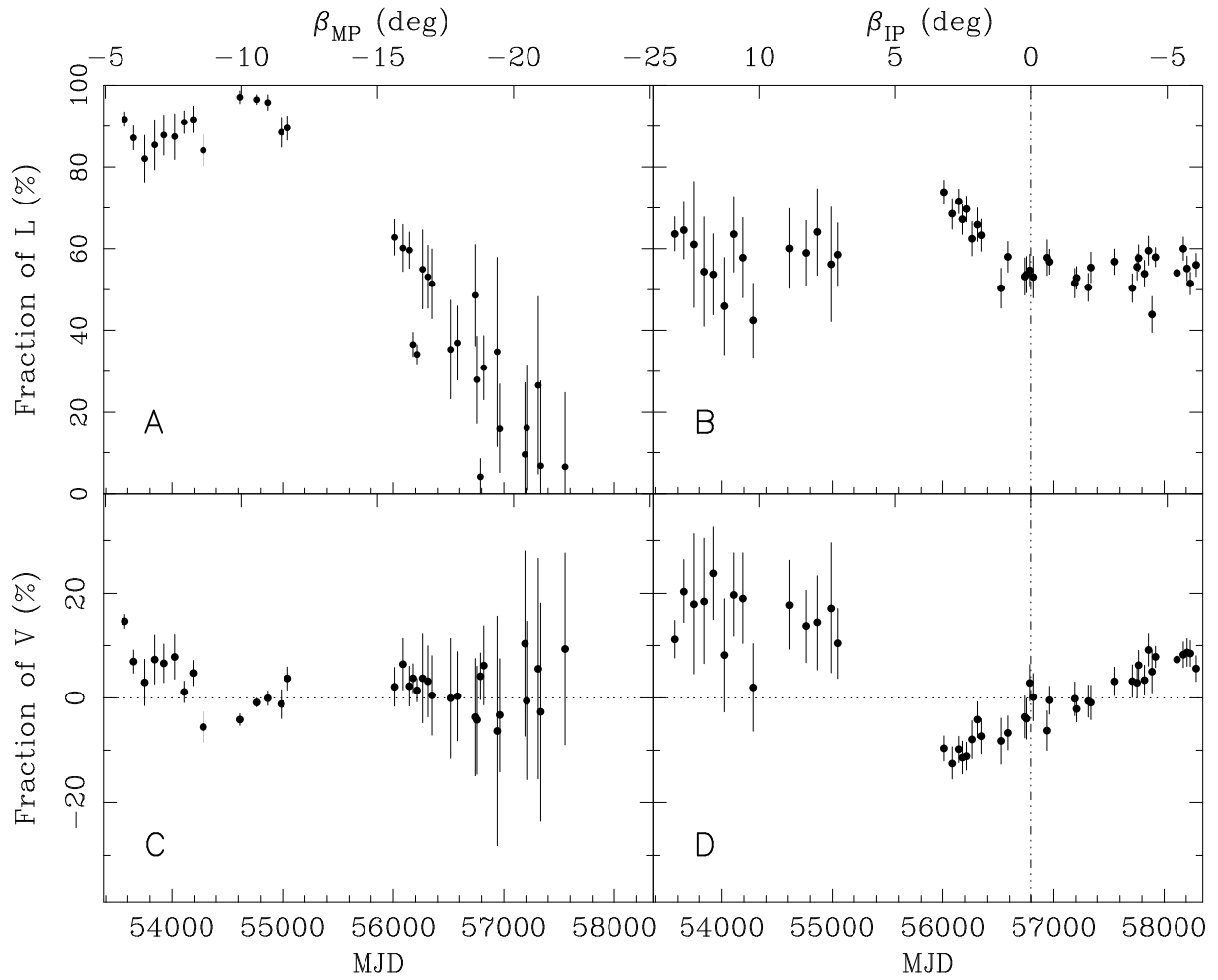


Figure S5: **Polarisation fraction of the pulse.** Average percentage of linear polarisation for the MP (A) and IP (B) and circular polarisation for the MP (C) and the IP (D) as a function of MJD (bottom x-axis label) and impact parameter  $\beta$  (top x-axis label).

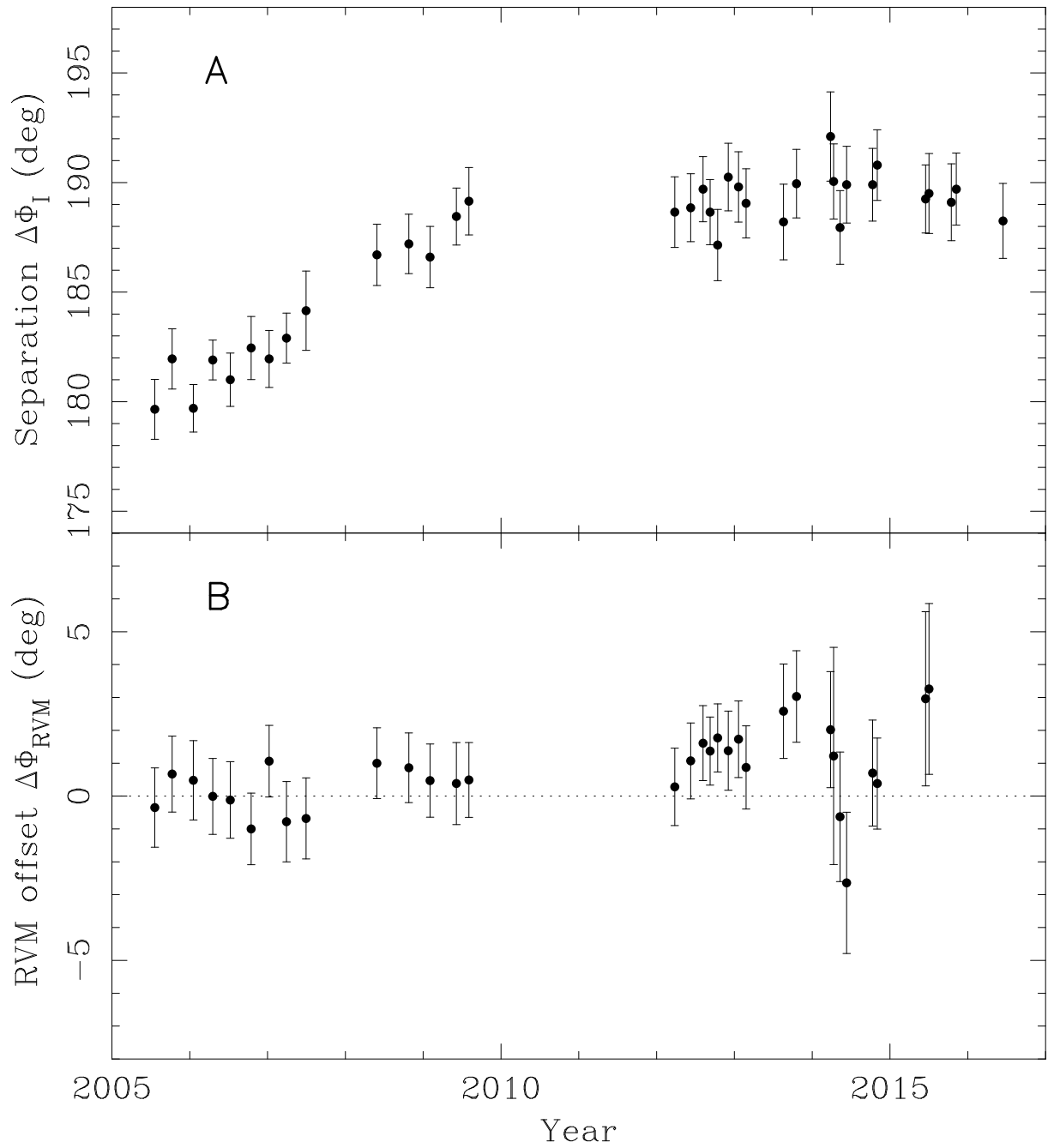


Figure S6: **Effects of different emission heights between the MP and IP.** (A) Separation  $\Delta\Phi_I$  between the MP and IP Stokes I midpoints. (B) Phase offset  $\Delta\Phi_{RVM}$  in the RVM curve between the MP and IP. The dashed line at  $0^\circ$  shows the expected value in case of the simple RVM (i.e. without considering rotational effects), or, when considering rotational effects, with the emission of the MP and IP originating at the same height.

Table S1: **Parameters of the ‘precessional RVM’.** Description of the parameters used in the ‘precessional RVM’, with the unit indicated in parenthesis. The values for  $\phi_{0\text{MP},k}$  with  $k \in \{1..47\}$  are not reported here as they are considered as ad-hoc alignment offsets in this model.

Parameter	Value	Description
$\alpha_{\text{MP}}$	$99.41 \pm 0.17$	Angle between the spin axis and the MP magnetic pole ( $^\circ$ )
$\delta$	$104 \pm 9$	Angle between the pulsar spin axis and the total angular momentum vector ( $^\circ$ )
$\Phi_0$	$249 \pm 10$	Reference precessional phase at epoch $T_0$ ( $^\circ$ )
$\Delta\psi_0$	$29 \pm 12$	Reference PA value at epoch $T_0$ ( $^\circ$ )
$\Omega_p$	$2.17 \pm 0.11$	Precession rate, can be set free or fixed to the value predicted by GR ( $^\circ \text{ yr}^{-1}$ )
$i$	$45 \pm 3$	Inclination angle, can be set free or fixed to the value predicted by GR ( $^\circ$ )
$\phi_{0\text{MP},k}$	—	Phase of the RVM inflection point of the MP for each epoch $k \in \{1..47\}$ ( $^\circ$ )

Table S2: **Summary of the observations.** Summary of the 47 epochs in our dataset. The columns show the MJD of the observation, backend name, integration time, estimated RM, impact parameter of the MP and IP as given by the individual RVM analysis, respectively. The MJD indicated for the BON data corresponds to the weighted MJD of the BON observations averaged together over a three month span. The RM of the ASP data is not reported here as the bandwidth of these data (16 MHz) is too small to derive a meaningful value.  $\beta_{\text{MP}}$  could not be reliably measured after MJD 56950 as the MP weakened until disappearance around MJD 57600-57700.

MJD	Backend	$T_{\text{int}}$ (hr)	RM ( $\text{rad m}^{-2}$ )	$\beta_{\text{MP}}$ (deg)	$\beta_{\text{IP}}$ (deg)
53571.9	BON	21.5	$155 \pm 7$	$-5.6^{+0.1}_{-0.1}$	$13.1^{+0.6}_{-0.6}$
53653.1	BON	12.0	$144 \pm 7$	$-6.7^{+0.2}_{-0.2}$	$11.6^{+0.8}_{-0.7}$
53752.6	BON	6.3	$153 \pm 6$	$-6.7^{+0.4}_{-0.5}$	$9.9^{+1.3}_{-1.1}$
53843.5	BON	2.3	$146 \pm 7$	$-6.7^{+0.6}_{-0.7}$	$13.3^{+2.1}_{-1.7}$
53925.8	BON	5.5	$159 \pm 7$	$-6.6^{+0.5}_{-0.6}$	$13.8^{+2.4}_{-1.9}$
54023.9	BON	3.5	$147 \pm 7$	$-6.8^{+0.6}_{-0.7}$	$14.7^{+2.4}_{-1.9}$
54108.4	BON	6.6	$149 \pm 6$	$-8.3^{+0.5}_{-0.5}$	$12.3^{+1.7}_{-1.4}$
54190.0	BON	8.0	$159 \pm 6$	$-9.2^{+0.6}_{-0.7}$	$11.8^{+1.7}_{-1.3}$
54281.8	BON	6.5	$153 \pm 8$	$-6.9^{+0.6}_{-0.7}$	$9.4^{+1.3}_{-1.1}$
54614.3	ASP	0.8	—	$-10.9^{+0.6}_{-0.6}$	$8.2^{+0.6}_{-0.6}$
54763.9	ASP	1.7	—	$-12.2^{+0.6}_{-0.6}$	$7.4^{+0.4}_{-0.4}$
54863.6	ASP	1.5	—	$-12.2^{+0.8}_{-0.8}$	$6.0^{+0.3}_{-0.3}$

Table S2 – *Continued from previous page*

MJD	Backend	T <sub>int</sub> (hr)	RM (rad m <sup>-2</sup> )	β <sub>MP</sub> (deg)	β <sub>IP</sub> (deg)
54987.3	ASP	1.1	—	-11.0 <sup>+1.7</sup> <sub>-1.9</sub>	6.6 <sup>+0.6</sup> <sub>-0.5</sub>
55046.1	ASP	1.2	—	-12.7 <sup>+1.3</sup> <sub>-1.4</sub>	6.2 <sup>+0.3</sup> <sub>-0.3</sub>
56012.4	PUPPI	2.1	150 ± 2	-19.0 <sup>+0.8</sup> <sub>-0.8</sub>	2.9 <sup>+0.1</sup> <sub>-0.1</sub>
56087.2	PUPPI	2.1	155 ± 3	-18.3 <sup>+1.0</sup> <sub>-1.1</sub>	2.7 <sup>+0.1</sup> <sub>-0.1</sub>
56145.1	PUPPI	2.2	156 ± 3	-21.0 <sup>+1.1</sup> <sub>-1.2</sub>	2.5 <sup>+0.1</sup> <sub>-0.1</sub>
56178.0	PUPPI	1.8	150 ± 3	-19.7 <sup>+1.1</sup> <sub>-1.3</sub>	2.3 <sup>+0.1</sup> <sub>-0.1</sub>
56213.9	PUPPI	2.2	152 ± 3	-19.4 <sup>+1.0</sup> <sub>-1.1</sub>	2.1 <sup>+0.1</sup> <sub>-0.1</sub>
56263.7	PUPPI	1.9	149 ± 3	-19.0 <sup>+1.3</sup> <sub>-1.4</sub>	1.9 <sup>+0.1</sup> <sub>-0.1</sub>
56311.6	PUPPI	2.2	157 ± 3	-18.2 <sup>+1.0</sup> <sub>-1.1</sub>	1.7 <sup>+0.1</sup> <sub>-0.1</sub>
56347.5	PUPPI	2.2	153 ± 3	-19.9 <sup>+1.2</sup> <sub>-1.3</sub>	1.8 <sup>+0.1</sup> <sub>-0.1</sub>
56523.0	PUPPI	1.8	154 ± 3	-19.3 <sup>+17.5</sup> <sub>-2.6</sub>	1.0 <sup>+7.4</sup> <sub>-0.1</sub>
56583.9	PUPPI	2.2	162 ± 3	-19.9 <sup>+1.5</sup> <sub>-1.8</sub>	0.6 <sup>+0.0</sup> <sub>-0.1</sub>
56743.4	PUPPI	1.6	155 ± 3	-19.5 <sup>+3.0</sup> <sub>-3.3</sub>	0.06 <sup>+0.04</sup> <sub>-0.03</sub>
56758.4	PUPPI	1.5	148 ± 3	-18.9 <sup>+4.3</sup> <sub>-4.4</sub>	0.04 <sup>+0.02</sup> <sub>-0.04</sub>
56788.3	PUPPI	2.0	149 ± 4	-13.4 <sup>+3.5</sup> <sub>-4.6</sub>	0.01 <sup>+0.02</sup> <sub>-0.02</sub>
56819.2	PUPPI	1.9	150 ± 4	-14.4 <sup>+18.7</sup> <sub>-6.8</sub>	0.00 <sup>+0.02</sup> <sub>-0.03</sub>
56940.9	PUPPI	2.1	154 ± 3	-15.6 <sup>+9.0</sup> <sub>-7.7</sub>	-0.34 <sup>+0.06</sup> <sub>-0.05</sub>
56962.8	PUPPI	2.2	154 ± 2	—	-0.44 <sup>+0.04</sup> <sub>-0.04</sub>
57190.2	PUPPI	1.7	153 ± 4	—	-1.3 <sup>+0.3</sup> <sub>-0.1</sub>
57206.2	PUPPI	1.9	153 ± 4	—	-1.3 <sup>+0.3</sup> <sub>-0.2</sub>
57310.9	PUPPI	2.1	158 ± 5	—	-2.0 <sup>+0.1</sup> <sub>-0.1</sub>
57333.8	PUPPI	2.1	153 ± 6	—	-2.0 <sup>+0.1</sup> <sub>-0.1</sub>
57553.2	PUPPI	2.2	148 ± 7	—	-3.2 <sup>+0.1</sup> <sub>-0.1</sub>
57712.8	PUPPI	1.8	157 ± 3	—	-3.7 <sup>+0.4</sup> <sub>-0.2</sub>
57755.6	PUPPI	1.8	153 ± 3	—	-3.7 <sup>+0.6</sup> <sub>-0.4</sub>
57769.6	PUPPI	1.4	153 ± 3	—	-4.0 <sup>+0.5</sup> <sub>-0.2</sub>
57822.5	PUPPI	1.3	152 ± 3	—	-4.4 <sup>+0.5</sup> <sub>-0.2</sub>
57858.4	PUPPI	1.8	152 ± 5	—	-3.9 <sup>+0.7</sup> <sub>-0.4</sub>
57890.3	PUPPI	1.3	149 ± 6	—	-4.2 <sup>+0.5</sup> <sub>-0.3</sub>
57921.2	PUPPI	2.1	152 ± 3	—	-4.7 <sup>+0.7</sup> <sub>-0.3</sub>
58116.7	PUPPI	1.2	154 ± 3	—	-5.7 <sup>+0.8</sup> <sub>-0.4</sub>
58174.5	PUPPI	1.5	153 ± 3	—	-5.6 <sup>+0.7</sup> <sub>-0.3</sub>
58207.5	PUPPI	2.0	153 ± 3	—	-6.1 <sup>+0.7</sup> <sub>-0.4</sub>
58237.4	PUPPI	2.0	151 ± 2	—	-5.2 <sup>+0.7</sup> <sub>-1.0</sub>
58290.2	PUPPI	1.4	152 ± 3	—	-6.2 <sup>+0.7</sup> <sub>-0.4</sub>